THESIS FOR THE DEGREE OF DOCTOR OF PHILOSOPHY

Spectroscopic investigation of palladium catalysts during wet methane oxidation

PETER VELIN

Department of Chemistry and Chemical Engineering

CHALMERS UNIVERSITY OF TECHNOLOGY

Gothenburg, Sweden 2020

Spectroscopic investigation of palladium catalysts during wet methane oxidation
PETER VELIN

Department of Chemistry and Chemical Engineering
Chalmers University of Technology
SE-412 96 Gothenburg
Sweden
Telephone +46 (0)31 772 1000

Spectroscopic investigation of palladium catalysts during wet methane oxidation

PETER VELIN

Department of Chemistry and Chemical Engineering

Chalmers University of Technology

Abstract

Abatement of the strong greenhouse gas methane in vehicle applications by use of catalytic end-of-pipe technologies is challenging due to the prevailing reaction conditions with low temperatures and high water content. In this thesis, the mechanisms behind low-temperature water inhibition of lean methane oxidation over palladium-based catalysts have been studied using an integrated experimental approach including wet-chemical preparation of model catalysts with systematic variation of key performance parameters, transient measurements of reaction kinetics in chemical flow reactor, and *operando* infrared and X-ray absorption spectroscopic characterisation.

For Pd/γ-Al$_2$O$_3$ catalysts, well developed PdO particles is the most active phase and the apparent activation energy for methane oxidation is significantly higher in presence of water. It increases with decreasing palladium particle size in the presence of water as opposed to dry conditions where it decreases slightly. Linear and bridge-bonded hydroxyl surface species on alumina evolve during dry methane oxidation by spill-over of hydrogen species to the PdO-Al$_2$O$_3$ rim, which correlates with a declining catalytic activity. Addition of water causes severe hydroxylation of the Pd/Al$_2$O$_3$ catalysts that significantly hamper the methane turnover frequency. On the contrary, for Pd/ZSM-5 catalysts, hydroxyl formation on the Pd-ZSM-5 rim can not be detected in dry conditions, and is minor upon water addition.

A high but not too high palladium dispersion, with palladium particle size not smaller than about 2 nm, is suggested for Pd/γ-Al$_2$O$_3$ catalysts as to balance water tolerance against palladium utilization. Lastly, ZSM-5 supported Pd-based catalysts show outstanding long-term performance for methane oxidation in the presence of water vapor compared to catalysts supported by γ-Al$_2$O$_3$. This finding stimulates the use of hydrophobic support materials given that palladium particles are sufficiently stabilized.

Keywords: Sustainable transports; Environmental catalysis; Methane oxidation; Supported palladium; Water inhibition; *Operando* spectroscopy; DRIFTS; XAS

List of Publications

This thesis is based on the following appended papers:

I. Palladium dispersion effects in wet methane oxidation

P. Velin, C.-R. Florén, M. Skoglundh, A. Raj, D. Thompsett, G. Smedler, and
P.-A. Carlsson

Submitted manuscript

II. Portable device for generation of ultra-pure water vapor feeds

P. Velin, U. Stenman, M. Skoglundh, and P.-A. Carlsson

Review of Scientific Instruments, **88** (2017), 115102-115109

III. Water inhibition in methane oxidation over alumina supported palladium catalysts

P. Velin, M. Ek, M. Skoglundh, A. Schaefer, A. Raj, D. Thompsett, G. Smedler, and
P.-A. Carlsson

The Journal of Physical Chemistry C, **123** (2019), 25724-25737

IV. Oxygen step-response experiments for methane oxidation over Pd/Al$_2$O$_3$: An in situ XAFS study

J. Nilsson, P.-A. Carlsson, N. M. Martin, P. Velin, D. M. Meira, H. Grönbeck, and
M. Skoglundh

Catalysis Communications, **109** (2018), 24-27

V. State of palladium during wet methane oxidation over Pd/Al$_2$O$_3$ and Pd/ZSM-5 catalysts

P. Velin, F. Hemmingsson, A. Schaefer, M. Skoglundh, K. A. Lomachenko, A. Raj,
D. Thompsett, G. Smedler, and P.-A. Carlsson

In manuscript

My Contributions to the Publications

Paper I

I had the leading role in planning and performing the experimental work. I analyzed most of the experimental data, interpreted the results and was together with Carl-Robert Florén in charge of writing the first draft of the manuscript.

Paper II

I was in charge of designing and constructing (not final assembling) the portable water generation device. I performed the experimental work and data analysis, interpreted the results with my co-authors and wrote the first draft and submitted the manuscript.

Paper III

I performed the experimental work (except for electron microscopy), data analysis, interpreted the results with my co-authors and wrote the first draft and submitted the manuscript.

Paper IV

I participated in sample preparation and collection of XAFS data at the European Synchrotron Radiation Facility and co-authored the manuscript.

Paper V

I participated in the collection of XAFS data at the European Synchrotron Radiation Facility, performed the remaining experimental work, data analysis, result interpretation and wrote the first draft of the manuscript.

Additional publications, not included in this thesis:

Characterization of surface structure and oxidation/reduction behavior of Pd-Pt/Al$_2$O$_3$ model catalysts
N. M. Martin, J. Nilsson, M. Skoglundh, E. C. Adams, X. Wang, P. Velin, G. Smedler, A. Raj, D. Thompsett, H. H. Brongersma, T. Grehl, G. Agostini, O. Mathon, S. Carlson, K. Norén, F. J. Martinez-Casado, Z. Matej, O. Balmes, and P.-A. Carlsson
The Journal of Physical Chemistry C, **120** (2016), 28009-28020

CO oxidation and site speciation for alloyed palladium-platinum model catalysts studied by *in situ* FTIR spectroscopy
N. M. Martin, M. Skoglundh, G. Smedler, A. Raj, D. Thompsett, P. Velin, F. J. Martinez-Casado, Z. Matej, O. Balmes, and P.-A. Carlsson
The Journal of Physical Chemistry C, **121** (2017), 26321-26329

Catalytic hydrogenation of CO$_2$ to methane over supported Pd, Rh and Ni catalysts
N. M. Martin, P. Velin, M. Skoglundh, M. Bauer, and P.-A. Carlsson
Catalysis Science & Technology, **7** (2017), 1086-1094

CONTENTS

CHAPTER 1

INTRODUCTION

Increasing atmospheric concentrations of greenhouse gases cause the Earth's temperature to rise [1]. A great challenge for mankind is thus to rapidly reduce anthropogenic emissions to acceptable low levels as to preserve the global average temperature within a bearable range and maintain ecological prosperity [2]. The shift from coal to natural gas in the heat and power generation sectors has in recent years led to reduced emissions of carbon dioxide (CO_2) in several developed economies [3]. Natural gas is, as the name implies, a naturally occurring resource with large reserves in the Earth's crust. It is a mixture of hydrocarbons that upon combustion generates the least amount of CO_2 per unit of energy released among all fossil fuels [4,5]. This is thanks to the high hydrogen-to-carbon ratio of the main constituent methane (CH_4) [6]. The shift to natural gas also benefits local environments as it burns cleanly with low emissions of nitrogen oxides (NO_x) and particulate matter [7]. Still, however, natural gas is a fossil fuel. The more sustainable approach would be to use a renewable source of methane, for example biogas that can be upgraded to natural gas standards by removing unwanted impurities such as CO_2, water, hydrogen sulphide, nitrogen, oxygen, ammonia and siloxanes [8]. Mixtures in any proportions are then possible, making methane rich fuels a plausible candidate in a future fuel mixture less dependent on conventional fossil fuels [9–11].

The transport sector is recognized as one of the main sources of atmospheric pollution. In 2017 it accounted for about a quarter of the global greenhouse gas emissions [12], and the public's concern about severe air pollution and health effects is rising. Thus, vehicle manufacturers consider methane rich fuels as a way forward to decreased

1

pollution. The methane rich fuels are especially applicable for long-haul heavy-duty trucks where the electrification of the powertrain is difficult to attain. Unfortunately, methane is a potent greenhouse gas itself with a global warming potential 28 times higher than that of CO_2 over a 100-year period [13]. To make use of the benefits of using natural gas and biogas fuels, methane emissions must be avoided. To do so, ever stricter emission regulations are implemented. In the Euro VI emission standard for heavy-duty vehicles, a methane limit of 0.5 g/km is set for the exhaust during transient testing. This is less than 50% of the allowed limit in Euro V (1.1 g/km) and indicates a more stringent trend [14]. As no combustion is ideal, there is always a risk of slip of methane from the engine, which follows the exhaust stream. To prevent methane and other pollutants from reaching the atmosphere, catalytic converters are installed in the exhaust system as an end-of-pipe solution. Particularly harmful emissions can thereby be converted into less harmful compounds over appropriate catalyst formulations and (to some extent) by controlling the operational conditions.

1.1   Environmental catalysis

Catalytic converters for vehicle emission abatement rely on heterogeneous catalysis. This means that the catalysts are solids, usually functionalised porous high-surface area materials that host the catalytic active sites, whereas the reactants and products are present in a fluid phase. In terms of chemical engineering this represents a diffusion-reaction system as during the catalytic process, the reactants/products are transported to/from the catalytic sites onto which the chemical reactions occur. For rapid reactions, the transport of reactants from the bulk fluid to the catalyst external surface (external mass transfer) or from the external catalyst surface to the active sites in the pores (internal diffusion) may control the overall rate [15, 16]. Thus, the overall conversion is not solely dependent on the intrinsic activity of the catalyst but also on the geometrical dimensions of the catalyst, e.g., substrate form and pore size, and the flow properties. This thesis concerns foremost understanding of intrinsic catalytic kinetics.

A catalyst is a material that increases the rate of a chemical reaction without being consumed. As illustrated in Figure 1.1a, a higher energy barrier must be passed to convert reactants to products for a gas-phase reaction as compared to the corresponding catalytic reaction where an alternative energetically more favourable pathway is pro-
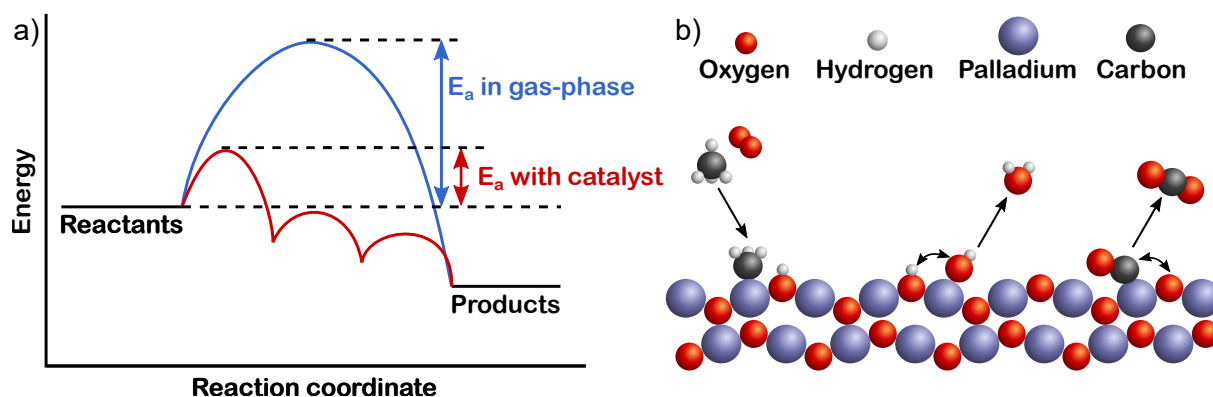
Figure 1.1: Illustration of a) the lower energy barriers for a catalysed reaction compared to the gas-phase reaction and b) some elementary steps of catalysed methane oxidation on a palladium oxide surface.

vided. The catalytic reaction path consists of several elementary steps that express how molecular bonds are rearranged to form a specific product [17]. A catalysed reaction is (usually) kinetically accelerated because intermediate reaction species are stabilised by the catalyst surface and the likelihood for collisions is higher on the surface than in gas phase. The overall change in energy, however, when reactants form products is the same whether or not a catalyst is present because it is dictated by the laws of thermodynamics. The overall rate for a catalytic reaction is commonly associated with the slowest elementary step, known as the rate-limiting step. To improve the function of the catalyst based on knowledge, it is important to understand the different processes involved in the product formation. Typical elementary steps for a heterogeneously catalysed reaction that need attention are reactant adsorption, surface diffusion, surface reaction between intermediates and product desorption, which are shown in Figure 1.1b. The illustrated steps in Figure 1.1b are taken from a detailed theoretical kinetic model that describes complete methane oxidation over an ideal palladium oxide surface, i.e., PdO(101) [18]. The PdO(101) surface has been identified as the most active palladium oxide surface for complete methane oxidation as it provides active sites with the lowest energy barrier for dissociative methane adsorption, which commonly is considered to be the rate-limiting step [19, 20]. Dissociative adsorption of methane to methyl and hydroxyl species is shown on the left hand side of Figure 1.1b. The methyl intermediate may then react further with under-coordinated oxygen atoms in the lattice according to a Mars-van Krevelen mechanism [18]. In order for the catalytic cycle to proceed, reoxidation of oxygen vacancies by oxygen adsorption and dissociation is required. Figure 1.1b illustrates surface reactions between two hydroxyl species (middle) and carbon

3

monoxide (CO) with a lattice oxygen (right). Desorption of the formed water and carbon dioxide adsorbates then occurs by breakage of the surface bonds to the products. At the heart of catalysis is to design active sites that possess a high intrinsic activity. In general, the high intrinsic activity is achieved when the interactions between reactant/product species and the active sites are neither too strong nor too weak [21]. A too strong interaction impedes surface diffusion and/or product desorption whereas a too weak interaction between reactants/intermediate will make the catalyst to fail to activate the reactants and facilitate collisions between surface intermediates. This is called the Sabatier principle.

Catalytic oxidation of methane is a challenging task. Even with the most efficient catalytic converters presently known, the desired methane conversion is often too low. A common explanation for this is the difficult activation of methane by the catalyst. This is due to the low sticking probability of methane, which is related to the highly symmetrical tetrahedral shape of the methane molecule with four nonpolar covalent bonds that withstands chemical attacks well [22, 23]. The most active catalyst formulations for complete oxidation of dilute methane are metal oxide supported noble metals, which have been used for decades. Thanks to their high thermal stability, high surface area and excellent mechanical strength, aluminium oxides (Al_2O_3), known as alumina, are commonly used as support material for palladium, sometimes promoted with platinum, in conventional abatement systems [24]. The palladium-alumina catalysts, however, are known to be susceptible to water vapor that strongly inhibits the methane oxidation reaction. This is a main challenge as large quantities (10–15 vol%) of water vapor are formed during methane combustion in the engine [25]. Figure 1.2a shows the dramatic
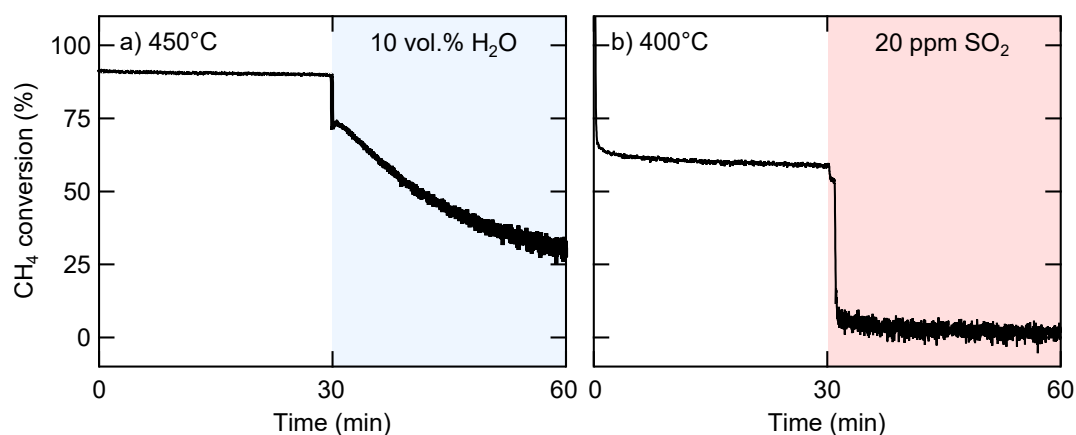

Figure 1.2: Effect of a) 10% H_2O and b) 20 ppm SO_2 on 0.1% CH_4 + 2% O_2 over Pd/Al_2O_3.

4

difference in methane conversion over a Pd/Al_2O_3 catalyst for dry and wet conditions. Initially in dry conditions, about 95% of the methane is converted to carbon dioxide. An initial rapid drop in methane conversion is observed upon introduction of water vapor followed by a slower continuous decrease to <35% during 30 min of exposure to 10 vol.% water vapor. The inhibiting effect of water vapor on methane oxidation over Pd/Al_2O_3 catalysts has been observed up to relatively high (550 °C) reaction temperatures, and no general agreement on how to explain the kinetic effects has yet been reached [25–28]. Some studies claim that the inhibiting effect is reversible and that the initially high catalytic activity can be regenerated by high-temperature treatment [29, 30]. This can, however, not serve as a main solution as the thermal sintering of palladium at high temperatures is too severe in the presence of water vapor [31–34]. In addition to water vapor, other detrimental compounds like sulphur and phosphorus oxides, may be present in the exhaust. Figure 1.2b shows that the presence of sulphur dioxide (SO_2), already in ppm level, can severely deactivate the catalyst. Unlike water vapor, which will always be present in the exhaust due to it being a combustion product, catalytic poisons such as SO_2 can to larger extent, although not completely, be avoided by implementing strict regulations of the fuel purity.

1.2   Research approach

In this work, a structured bottom-up approach has been implemented to examine the inhibiting effect of water vapor on methane oxidation for Pd-based catalysts in oxygen excess. The individual components (active and support material) of the model catalysts were studied independently as well as combined understand complications that may arise from interactions between the active phase and support. Various model catalysts with relatively low complexity were prepared using different Pd loadings, Pd precursor solutions, calcination temperatures and support materials with the aim to understand how catalyst properties impact the function of the catalyst. Working with simplified catalyst formulations is in one sense a way to bridge the materials gap between complex industrial catalysts and well-defined surfaces of single crystals. Physicochemical findings may then be utilized to develop fully formulated catalysts with high complexity targeted to better sustain high performance in specifically harsh conditions.

Four experimental key steps, represented in Figure 1.3, were put into practice in the
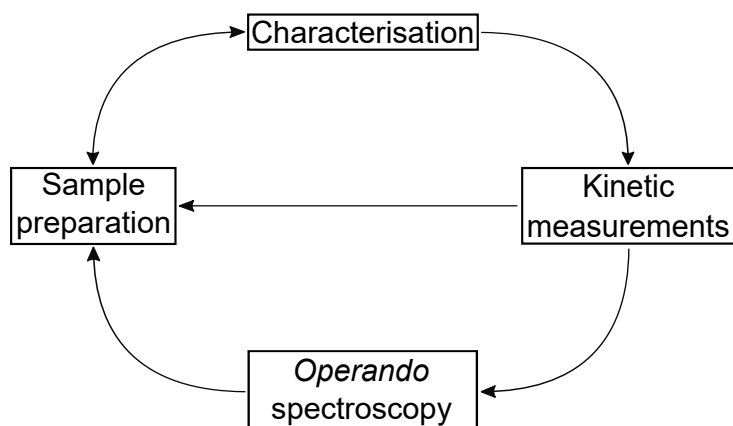
Figure 1.3: Schematic representation of the main steps used in this thesis to study catalytic methane oxidation. Successful sample preparation is confirmed by physicochemical characterisation and preparation of new catalysts is guided by both kinetic analysis and *operando* spectroscopy measurements.

strive to build understanding of the mechanisms behind water inhibition. The first step is sample preparation that includes, on the one hand, preparation of powder samples of palladium oxide and support materials and, on the other hand, syntheses of supported powder and monolith catalysts. Charaterisation of the physicochemical properties of the prepared samples was then made in a second step as to investigate whether or not the preparation was successful. If an important property of the sample, e.g., palladium loading or dispersion was poor, the preparation was either repeated or the type of sample formulation was disregarded. For samples that turned out to have compelling properties, kinetic evaluation of catalytic activity and selectivity was performed in a third step. The fourth step concerns *operando* spectroscopy. The term *operando* spectroscopy generally emphasizes that spectroscopic data is collected in experiments carried out under (relevant) reaction conditions and that the performance of the material under study is evaluated simultaneously [35, 36]. In the field of heterogeneous catalysis, this allows for correlation of catalyst structure and surface species with apparent catalytic reaction kinetics. Knowledge of such catalyst structure-function relationships is highly valuable when designing new efficient catalyst formulations for certain environments, such as catalysts for methane oxidation in the presence of water vapor.

1.3   Objectives

The aim of this thesis is to bring forward mechanistic explanations for the observed water inhibition of methane oxidation over supported palladium-based catalysts at conditions relevant for methane emission control and based on these findings propose new catalyst formulations with increased water tolerance.

CHAPTER 2

THE MODEL CATALYST

Commercial catalysts designed for real applications often have a rich structural variation that hinders mechanistically conclusive studies. Unlike commercial catalysts, model catalysts are prepared to achieve (sufficient) structural control with the purpose to facilitate deep investigations and building of knowledge of relevant phenomena. The gained insights can then be applied to improve existing catalyst formulations and their synthesis or develop new catalyst concepts [37]. The model catalysts in this work are simplified versions of commercial ones that have been prepared by industrially relevant scalable methods. This chapter describes first the methods used for preparation of model catalysts and then the techniques used for basic catalyst characterisation together with some key findings. The final part contains a summary in tabular form of the most important properties for all catalysts used in this thesis.

2.1 Catalyst preparation

Catalyst manufacturing techniques are continuously developed as to improve catalyst formulations for established processes and enable new reaction routes. Some of the most frequently used techniques today are incipient wetness impregnation (IWI), precipitation, sol-gel processing, hydrothermal synthesis and templating [38]. The powder catalysts prepared in this work were synthesised by incipient wetness impregnation also known as dry impregnation. This is one of the most common preparation methods used for industrial production of supported catalysts thanks to its relative simplicity and low
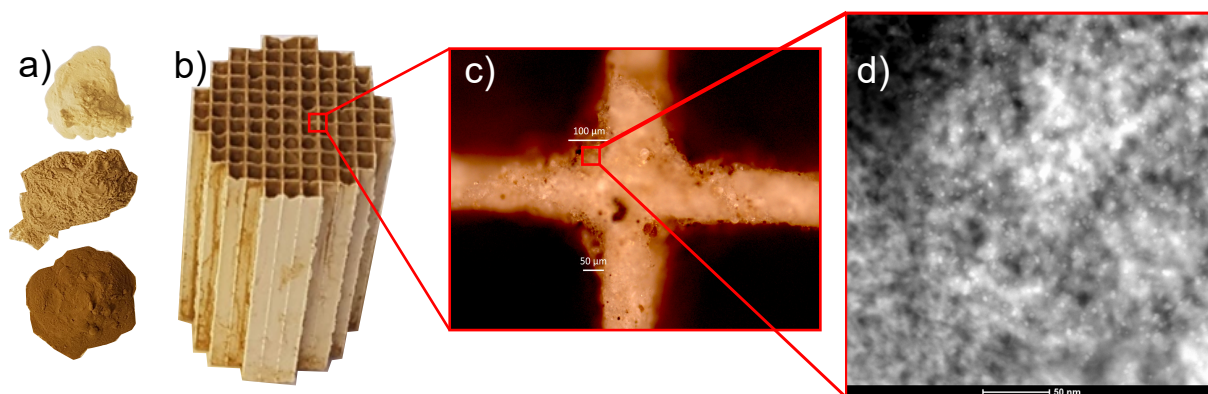
Figure 2.1: a) Pd/Al_2O_3 powders samples with 0.25, 1 and 2 wt% palladium, b) a ceramic monolith substrate coated with Pd/Al_2O_3, c) optical microscopy image of the coated monolith cross-section, and d) electron microscopy image of a Pd/Al_2O_3 washcoat used in reactor experiments.

waste production streams [39]. In some cases the powder catalysts were applied onto ceramic monolith substrates by washcoating.

2.1.1 Incipient wetness impregnation

The incipient wetness impregnation method involves three basic steps starting with thorough mixing of the support material with the precursor solution that contains the elements for the active phase. To enable a high dispersion of the active phase, the added volume of precursor solution should be equivalent to the pore volume of the support material. When saturation is reached, the mixture obtains a paste consistency. The sample paste is then dried as to remove the absorbed liquid from the pores. The dried powder is subsequently activated by calcination at high temperature for a certain period of time.

The chemistry occurring during the IWI preparation depends on many parameters that can be optimized as to attain the desired impregnation profile. The final active metal dispersion is strongly influenced by interrelated parameters of the reacting system such as pH, viscosity, precursor complex type and concentration, and choice of counter ions [38]. A high interaction strength between the support and the metal precursor complex is important, and can be facilitated by adjusting the pH of the solution. By matching the charge of an active metal complex in a solution with a support surface of an opposite charge, electrostatic interactions are created [40]. This requires knowledge about both the charge of the complex and the isoelectric point of the support, i.e.

the pH at which the surface charge is zero [41]. The model catalysts used in this thesis have been prepared using knowledge gained after rigorous synthesis optimization. Thereby catalysts with high control of the palladium dispersion for different supports and palladium loadings could be prepared.

The main support material in this work is γ-Al$_2$O$_3$ and to some extent ZSM-5 with a high silica to alumina (SAR) ratio of approximately 2000. Other support materials such as silica, cerium oxide, boron nitride and silicon carbide have also been used but just occasionally and are not included in the thesis. Catalysts with palladium loadings varying from 0.25 to 4 wt.% were prepared using different amounts of palladium precursor solutions. Figure 2.1a, shows the color gradient with increased palladium loading (0.25, 1 and 2 wt.% Pd) for some typical Pd/γ-Al$_2$O$_3$ powder samples. Thermal treatment of the powder samples in air was performed at temperatures ranging from 500 to 900 °C for several durations. A set of model catalysts with different palladium loadings but similar palladium areas was prepared by controlled thermal treatment with matched temperatures and durations.

2.1.2   Washcoating of monolith substrates

Some of the prepared powder catalysts were washcoated onto honeycomb structured cordierite monolith substrates (Corning, 400 cpsi, L=20 mm, $\varnothing$=14) for kinetic experiments in a flow reactor. A slurry of catalyst powder and a suitable binder material was first mixed in a 50/50 solution of Milli-Q water and ethanol. The monolith substrate was immersed in the slurry and the channels were filled by capillary forces. The monolith was then dried under a heating gun in air at about 100 °C for 2 min, followed by calcination at about 500 °C for 2 min. The coating procedure was repeated until 200 mg of solid had been coated onto the monolith. Finally, the coated monoliths were calcined in a furnace at 500 °C for 2 h in air. Figure 2.1b shows a monolith substrate coated with a Pd/Al$_2$O$_3$ powder sample with 1 wt% palladium. Optical microscopy imaging shown in Figure 2.1c clearly indicates that the coating is thicker in the corners than on the sides of the monolith channels. A uniform coating is one of the challenges encountered during washcoating. Other issues may arise due to blockage of pores and active sites, poor adhesion, cracking and loss of catalyst over time.

2.2 Catalyst characterisation

Thorough catalyst characterisation plays a vital role for the interpretation of kinetic measurements and to build fundamental understanding of the catalytic system at hand. Today numerous analysis techniques are available. Here, the techniques used for determination of elemental composition, specific surface area, active metal dispersion, palladium particle shape and catalyst structure are described. The gained physicochemical knowledge has been essential for interpreting the kinetic and spectroscopic results presented further on.
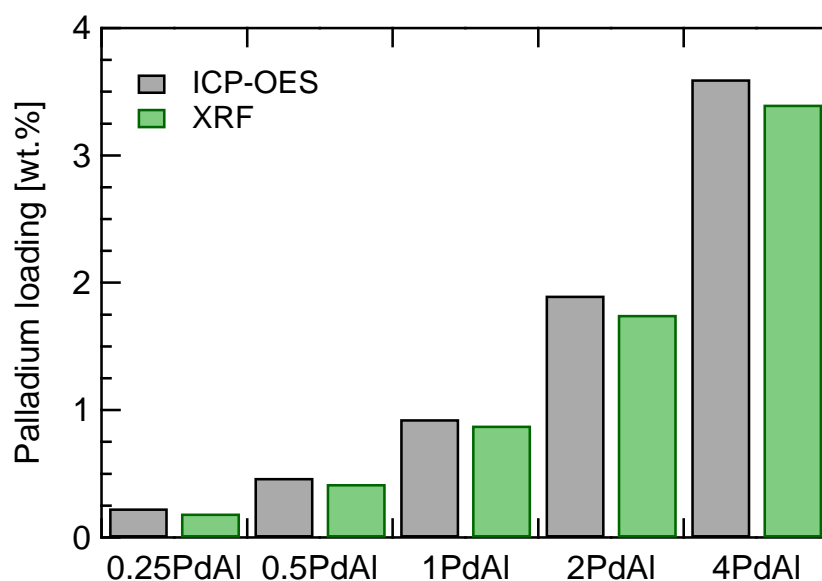
2.2.1 Composition

Quantitative analysis of the elemental composition of a catalyst can be achieved by a variety of methods. In this work, inductively coupled plasma optical emission spectrometry (ICP-OES) and X-ray fluorescence (XRF) measurements have been used to determine the palladium loading of the catalysts. When used properly, the two techniques are capable of giving excellent accuracy and precision.

ICP-OES measurements

To determine the palladium content of a sample with ICP-OES, about 30 mg of powder sample was first digested in aqua regia at 180 °C in a microwave oven. By spraying the sample solution as an aerosol directly through a plasma flame, all molecules break down into charged ions. The characteristic wavelengths of the radiation that is emitted when the ions recombine to their ground state was measured [42]. Quantitative determination of the palladium loading was finally obtained by comparing the intensity with calibration standards of known elemental compositions.

XRF measurements

X-ray fluorescence is similarly to ICP-OES an atomic emission method where the wavelength and intensity of emitted radiation from energized atoms are measured [43]. Prior to elemental analysis, pellets were prepared by mixing 0.5 g of powder sample with 2.7 g of binder material (SpectroBlend™, Chemplex Industries Inc). To achieve a highly homogeneous mixture, the powders were thoroughly mixed for 10 min. The mixture was then pressed to pellets under a pressure of 14 bar. The pellet was then placed

Figure 2.2: Elemental analysis of palladium by Inductively coupled plasma optical emission spectrometry and X-ray fluorescence.

in a sample holder in the instrument and subsequently radiated with high-energy X-ray radiation. Electrons from inner orbitals are then ejected, which leads to the formation of an unstable electronic structure with electron holes. When electrons in higher orbitals falls back to the electron holes, fluorescent radiation of characteristic energies is emitted from the elements present in the sample. Calibration standards of known elemental composition are hence also with this technique required for quantitative analysis.

As for all techniques potential sources of error exist. The bar graph of Figure 2.2 compares the elemental analysis of palladium for a series of Al_2O_3 supported catalysts prepared to be impregnated with 0.25, 0.5, 1, 2 and 4 wt.% palladium. The analyses confirm that the palladium loading is fairly close to target. A systematic error is however indicated for the XRF method, which results in a slightly lower measured elemental concentration of palladium compared to ICP-OES.

2.2.2 Specific surface area

The specific surface area (SSA) is defined as the total surface area per unit of mass and is an important physical property to consider when choosing a support material for a catalyst. The catalytic conversion is governed by a higher number of active sites. To achieve this, a high SSA of the support is advantageous as it provides a high surface
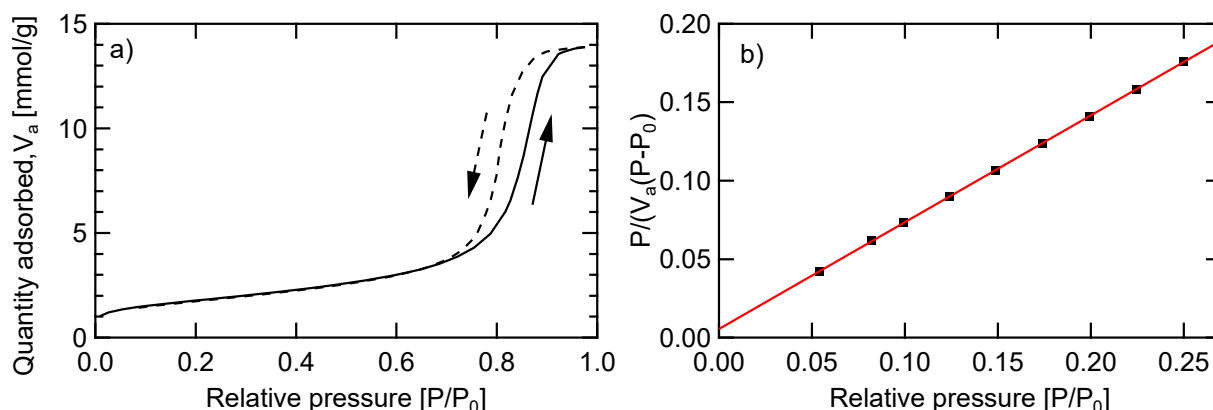
Figure 2.3: a) Nitrogen adsorption and desorption isotherms for a porous solid (Pd/Al$_2$O$_3$). b) Example of a BET plot.

area onto which the active metal can be dispersed. The SSA is determined by nitrogen physisorption. This method mainly involves weak interaction between the adsorbent and adsorbate *via* van der Waals forces. Prior to analysis, about 150 mg of sample was added to a quartz tube and dried at 225 °C for 3 h in a flow of nitrogen gas to get the actual dry weight of the sample. The quartz tube with the dried sample was then mounted in the instrument (Micromeritics, ASAP 2020 Plus) where it was cooled to -196 °C in liquid nitrogen. The molar quantity of gas adsorbed (V$_a$) was monitored while the relative pressure of nitrogen (P/P_0, where P is the actual gas pressure and P_0 is the vapor pressure of nitrogen) was increased step-wise from close to 0 to close to 1. The relative pressure was finally decreased from close to 1 to close to 0. For mesoporous materials like the Pd/Al$_2$O$_3$ catalyst, the plot of adsorbed nitrogen *versus* relative pressure creates an adsorption/desorption isotherm with a hysteresis as shown in Figure 2.3a.

In addition to the physisorption measurements, a theoretical method known as the BET theory from the surnames of its originators Brunauer, Emmett and Teller, is required for SSA determination [44]. The BET theory is a generalized approach of the Langmuir adsorption model, which describes the equilibrium between molecules in gas phase and molecules adsorbed on a surface [45]. The BET approach also treats multilayer adsorption and compared to the Langmuir model, a few more assumptions must be fulfilled [46, 47]:

- The adsorbent surface is uniform.
- The adsorption energy is constant for the first layer and equals the molar heat of

condensation for all layers except the first.

- The top layer is in equilibrium with the gas phase.
- The number of adsorption layers approaches infinite when the actual pressure equals the vapor pressure.

The SSA of the adsorbent can be calculated using equation 2.1. Here, V_m is the quantity of gas adsorbed to form a monolayer, σ is the area of the surface occupied by a single adsorbed gas molecule, N_A is the Avogadro constant, m is the mass of the adsorbent, and V_0 is the molar volume of the gas:

$$SSA = \frac{V_m \sigma N_A}{m V_0} \tag{2.1}$$

In the case when nitrogen is used as the adsorbate, equation 2.1 can be simplified to:

$$SSA_{N_2} = \frac{4.35 V_m}{m} \tag{2.2}$$

The V_m can be obtained from the slope and intercept of the regression line in the BET plot, see Figure 2.3b. The BET plot relates to the BET equation, which is written in its linear form in equation 2.3, where C is a constant:

$$\frac{P}{V_a(P_0 - P)} = \frac{C-1}{V_m C}\frac{P}{P_0} + \frac{1}{V_m C} \tag{2.3}$$

2.2.3 Palladium dispersion

A high dispersion of the active metal is desirable to create many catalytic sites and utilize the included active component well. Dispersion is the relation between surface and bulk atoms of the elements in question. To determine the number of active sites one commonly uses selective chemisorption methods. Contrary to the physisorption measurements, chemisorption is an activated process where the net heat of adsorption increases with increased temperature [47]. The technique relies on strong interaction between the chemisorbed adsorbate and the active metal atom(s), typically involving the sharing of electrons. The chemisorbed layer is assumed to not exceed a single molecule thickness [48].

CO chemisorption measurements

Carbon monoxide chemisorption measurements were used to determine the palladium dispersion (D_{Pd}), area (A_{Pd}) and particle size (d_{Pd}) for the model catalysts. To ensure
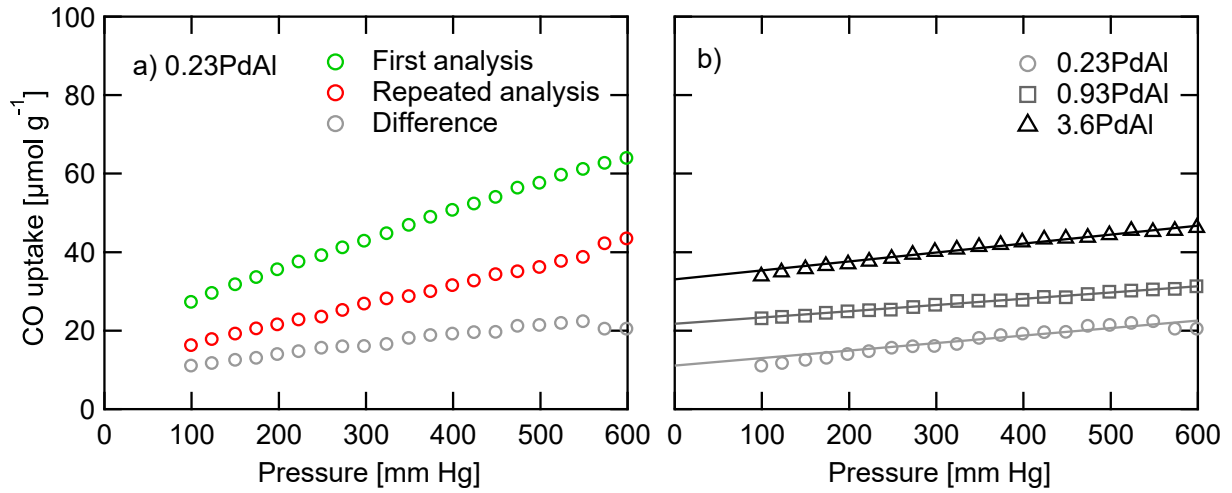
Figure 2.4: a) Isotherms generated by volumetric chemisorption of carbon monoxide at 35 °C over a Pd/Al$_2$O$_3$ catalyst with 0.23 wt% Pd. Green and red circles represent the first and repeated analysis, respectively while grey circles represent the difference between the two analyses. b) Examples of the difference isotherms for Pd/Al$_2$O$_3$ catalysts with 0.23, 0.93 and 3.6 wt% Pd.

reliable and reproducible results, the samples were prior to analysis oxidised, reduced and evacuated at 500 °C for 1 h per step. The temperature was then decreased to 35 °C and the reduced active metal was exposed to CO using pressure increments of 25 mm Hg between 100-600 mm Hg. After each increment, the pressure was allowed to settle equilibrium and the adsorbed quantity was measured. The analysis was repeated once to obtain a second isotherm, see Figure 2.4. The first adsorption isotherm is considered to include both chemisorbed and physisorbed CO while the second isotherm is assumed to be reversible and only include physisorbed CO. By subtracting the second isotherm from the first, an approximation of the chemisorbed CO is represented as a plateau. The volume of the chemisorbed monolayer of CO on the active surface (V_{Chem}) was then determined by extending a line from the plateau to the y-axis. Figure 2.4b shows three examples of the chemisorbed isotherm for Pd/Al$_2$O$_3$ catalysts with different palladium loadings.

The palladium dispersion was determined using the volume of the chemisorbed CO monolayer (V_{Chem}) according to:

$$D_{Pd} = \frac{V_{chem} W_A F_S}{V_{mol} M} 100\%$$ (2.4)

where W_A is the atomic weight of the metal, V_{mol} the molar volume of the adsorbate, M the percent of active metal by weight in grams per gram of sample, and F_S the stoichiometry factor. F_S is the ratio of the number of active surface atoms interacting

with one adsorbed molecule. For a chemisorbed molecule like carbon monoxide that binds in multiple configurations (linear and bridge bonded) to the surface depending on the structure of the surface [49–51], the F_S is not always easy to determine. Typical literature values assume F_S to be 1 or 2. In this work, however, a thorough method involving infrared CO chemisorption measurements and deconvolution of the carbonyl vibrational bands was implemented to determine F_S as detailed in section 4.2.3.

The active palladium area (A_{Pd}) of the sample is another concept that has been used when comparing the performance of different catalysts. A_{Pd} is expressed in the unit m^2/g sample and reflects the palladium area accessible for reactants to adsorb and transform on. It can be determined by:

$$A_{Pd} = n_a F_S a_s N_A \tag{2.5}$$

where V_{Chem} (determined from the adsorption isotherms) instead is expressed as the number of mole of gas adsorbed in a monolayer (n_a). The cross-sectional area (a_s) of the chemisorbed molecule is also needed.

A third way to use chemisorption measurements is by estimating the average active particle diameter (d). For the palladium particles used in this thesis, a hemispherical geometry has been assumed, which was confirmed by electron microscopy (see section 2.3.4). In this case, the palladium particle diameter d_{Pd} is calculated according to:

$$d_{Pd} = \frac{9}{A_{Sm}\gamma\%\rho}(100) \tag{2.6}$$

using the active metal area per gram of pure metal (A_{sm}), the metal density (ρ), the area-to-volume ratio ($9/d$), and the metal dispersion (D).

Figure 2.5 shows an example where the palladium area is plotted versus the palladium loading for a series of model catalysts were the elemental palladium composition varies from 0.23 to 3.6 wt.%. An increased palladium area with palladium loading is observed for the powder samples. At high palladium loadings, the increase in palladium area is somewhat stalled. This indicates that the palladium area approaches a plateau, and that the preparation of catalyst with higher loadings will not improve the catalytic performance significantly. Furthermore, the trends observed for the coated monolith samples in Figure 2.5 reveal a large drop in palladium area compared to the powder samples. This is likely due to a poor coating procedure where both active sites and pores are blocked.
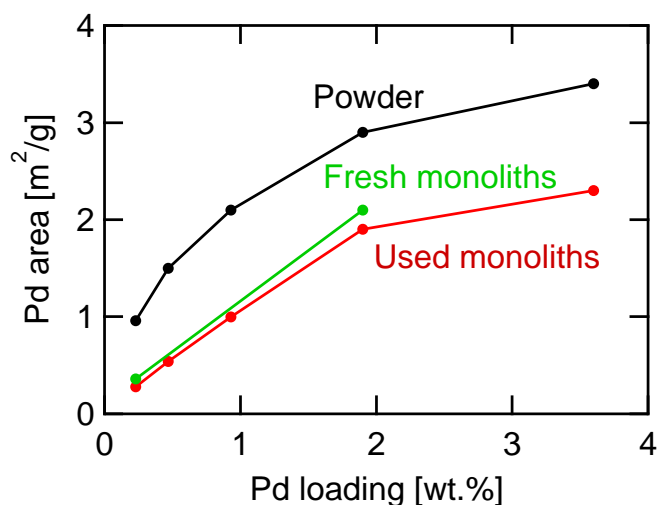
Figure 2.5: Palladium area plotted versus the palladium loading for powder samples, fresh monoliths and used monoliths.

2.2.4 Particle size and shape

As mentioned in the previous section, assumptions of a specific particle shape is required to determine the particle size by chemisorption measurements. To find out the true shape and size, imaging with microscopic methods can be applied. One such technique is scanning transmission electron microscopy (STEM), which has been used in this work to learn more about palladium particles dispersed on alumina. In STEM measurements, electromagnetic lenses are used to focus the electron beam to create a small probe which is scanned over the sample. Transmitted electrons, scattered with a large angle are then detected. This technique is called high-angle annular dark-field (HAADF-STEM) and it allows for a very high resolution to be used [52]. The detected intensity is a function of the atomic number of the element and heavier elements hence appear brighter. Prior to STEM imaging, the catalyst powder was mixed with ethanol and dispersed onto a Lacey carbon copper grid. The grid was then dried for at least 60 minutes before placed in the sample holder in the microscope.

HAADF-STEM measurements

Palladium particles dispersed on γ-Al_2O_3 are observed as bright spherical spots in Figure 2.6. For a Pd/γ-Al_2O_3 catalyst calcined at 500 °C, numerous of small particles with diameters from 1 to 5 nm are observed in Figure 2.6a. An average particle diameter of 2.4 nm ($N = 227$) correlates relatively well to CO chemisorption measurements
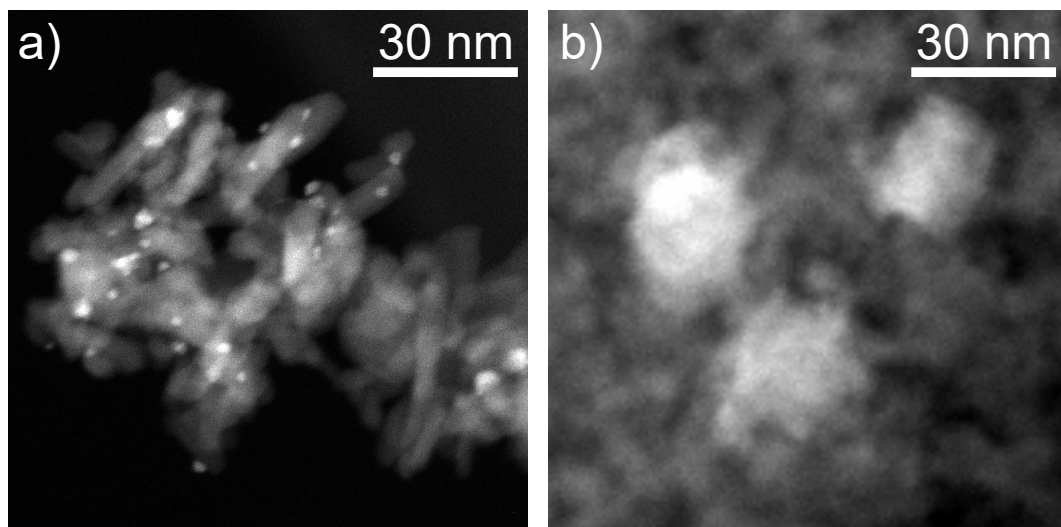
Figure 2.6: HAADF-STEM imaging of Pd/γ-Al$_2$O$_3$ catalysts calcined at 500 °C (a) and 900 °C (b).

(d_{Pd} = 3.4 nm). The slightly smaller particle size observed with electron microscopy imaging is likely due to palladium incorporation by the γ-Al$_2$O$_3$ support, making parts of the active surface inaccessible. A significantly increased particle size is revealed in Figure 2.6b for a catalyst calcined at 900 °C. The sintered palladium particles are here adapted to the morphology of the surrounding support. The average size of the agglomerated palladium particles for this sample is equivalent to a spherical diameter of 32 nm (N = 228). This is larger than estimated by CO chemisorption, which likely originates from the uneven, high surface area morphology of the agglomerates. Chemisorption is also highly sensitive to unsintered palladium particles and atomic clusters that are difficult to detect by electron microscopy.

Oxidised *versus* reduced palladium particles
The impact of reduction on PdO particle size and shape was studied with *in situ* STEM. For these measurements, the catalysts were ground and dry dispersed onto microelectromechanical systems (MEMS) heating chips. The samples were first heated in vacuum to 500 °C in the electron microscope. Hydrogen was subsequently introduced to the sample compartment while keeping the temperature at 500 °C. As demonstrated in Figure 2.7, the palladium particle size is minimally changed when a particle is reduced by hydrogen from an oxidised state. Some minor changes are however observed and highlighted with black and white arrows in Figure 2.7a and b. The white arrows indicate that some particles on the Pd/γ-Al$_2$O$_3$ catalyst calcined at 500 °C merge in the pres-
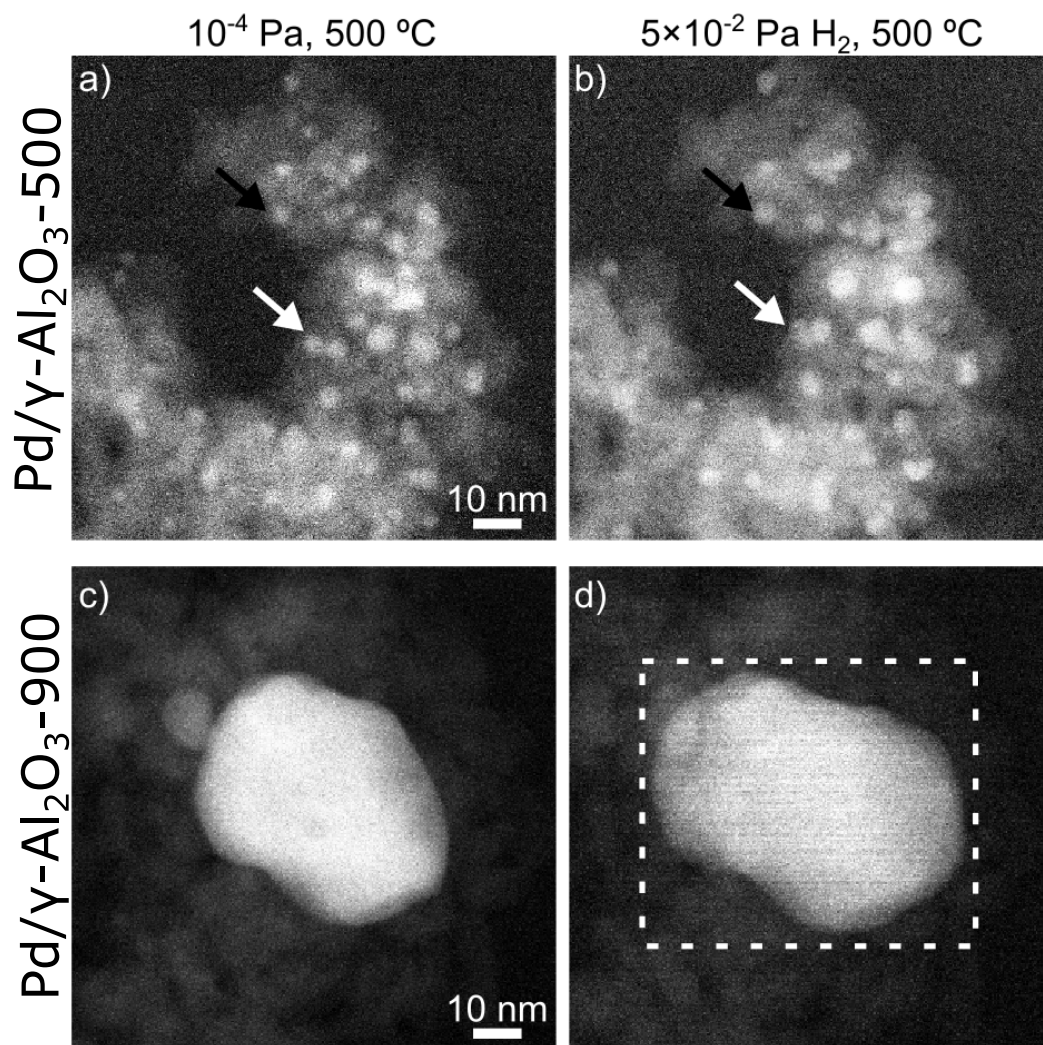
Figure 2.7: *In situ* STEM micrographs of a Pd/γ-Al$_2$O$_3$ catalyst calcined at 500 °C (a and b) and 900 °C (c and d) acquired while heating the catalysts in vacuum to 500 °C (a and c) and in 0.05 Pa of H$_2$ at 500 °C (b and d).

ence of hydrogen. The black arrows capture another trend where a particle increases in size even though it does not merge with any neighbouring particles. The latter trend was also observed for the Pd/γ-Al$_2$O$_3$ catalyst calcined at 900 °C in Figure 2.7c and d. When exposed to reducing conditions, the formed Pd agglomerates appear to spread a bit more over the support. Similar re-shaping has been reported for larger single crystalline particles by Zhang et al. [53]. These results support that CO chemisorption can be used as a good measure of the PdO particle size, although not measured in an oxidised state as the catalyst is supposed to operate in.

2.2.5 Crystalline phases

Powder X-ray diffraction (XRD) is employed to determine bulk crystalline structures of matter. It relies on the scattering of X-rays caused by their interaction with matter. The wavelength (λ) of the radiation should be in the same order of magnitude as the length of the periodic spacing (d_{hkl}) between crystal planes for a useful interaction to occur. Laboratory X-rays are typically produced by acceleration of an electron beam onto a metal, for example onto copper resulting in an X-ray beam with a wavelength of 0.154 nm. Undesired frequencies are filtered away using a nickel filter. A diffraction pattern will be obtained only at specific incident angles when elastically scattered X-rays from different planes are in phase, i.e. when constructive interference is fulfilled. Figure 2.8 illustrates the reflection of monochromatic X-rays (A and D) by a crystal. The ray denoted A is scattered by the atom at position B while ray D is scattered by the atom at F. Their incident angle to the lattice planes with Miller indices *hkl* and the interplanar spacing d_{hkl} is θ. For the reflected X-rays to emerge as a beam with higher intensity, constructive interference has to take place. This means that the difference in path length (EF + FG) has to equal an integer number (n) of the wavelength λ. Since the path length EF and FG equal each other as well as $d_{hkl}sin\theta$, the difference in path length can be written $2d_{hkl}sin\theta$. Bragg's law (equation 2.7), can accordingly relate interplanar spacings to diffraction peaks at specific incident angles:

$$n\lambda = 2d_{hkl}sin\theta \tag{2.7}$$
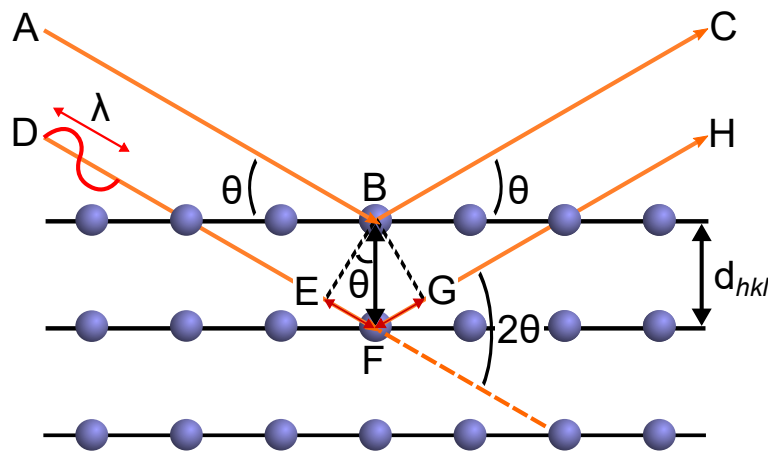
**Figure 2.8:** Schematic representation of the Bragg reflection of X-rays by a crystal with the interplanar spacing d_{hkl}.

The width of the diffraction peak decreases as the crystallite size increases. This is due to a more complete destructive interference for larger crystallites compared to smaller ones where a deficiency in lattice planes broadens the peak. The effect is used in the Debye-Sherrer equation (2.7) to estimate the mean crystallite size (τ). Here, β is the the full width at half maximum of the diffraction peak and κ is a dimensionless shape factor:

$$\tau = \frac{\kappa \, \lambda}{\beta \, cos\theta} \tag{2.8}$$

XRD measurements

Prior to XRD measurements, the catalyst powder sample was added to a sample holder and a piece of glass was used to flatten the surface to achieve a smooth top layer. The measurement was then performed by irradiating the powder sample with monochromatic X-rays and varying the incident angle (θ) from 20 to 70 °. The sample holder was rotated throughout the measurement with 15 revolutions per minute as to cover a larger sample area and improve the statistics. The X-ray diffractograms in Figure 2.9 show that the Pd/γ-Al$_2$O$_3$-500 sample has an almost identical diffraction pattern as bare γ-Al$_2$O$_3$. This indicates that a majority of the PdO particles are too small (and/or amorphous) for diffraction to occur. This interpretation agrees well with both CO chemisorption and STEM analysis. The pure PdO and Pd/γ-Al$_2$O$_3$-900 powder samples contain sufficiently
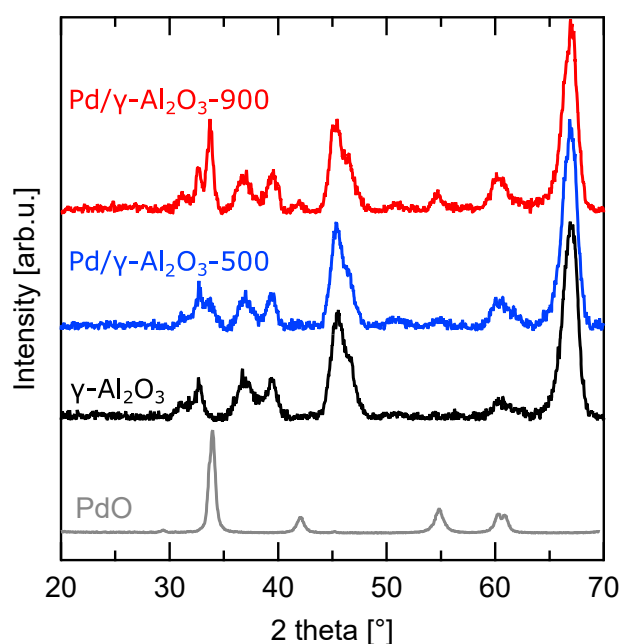
Figure 2.9: X-ray diffraction patterns of PdO (grey), γ-Al$_2$O$_3$ (black), Pd/γ-Al$_2$O$_3$-500 (blue) and Pd/γ-Al$_2$O$_3$-900 (red).

large and crystalline PdO particles as to give rise to distinct PdO reflections. From the diffraction peak at approximately 34 ° and using the Debye-Sherrer formula, a mean PdO particle diameter of 17 and 11 nm was estimated for PdO and Pd/γ-Al$_2$O$_3$-900, respectively. The PdO particle size calculated for the model catalyst was larger than measured for reduced particles by CO chemisorption, but smaller than observed with electron microscopy.

2.3 Summary of model catalysts

Table 2.1 shows the denoted sample ID's of the model catalysts used in this thesis along with physicochemical properties.

Table 2.1: Sample ID, calcination conditions, Pd loading, specific surface area (SSA), Pd dispersion (D_{Pd}), specific Pd area (A_{Pd}), Pd particle diameter (d_{Pd}), and apparent PdO particle size (d_{PdO}) shown for the powder samples used in this thesis.

| Sample ID	Calcination	Pd load [wt.%]	SSA [m^2/g]	D_{Pd} [%]	A_{Pd} [m^2/g]	d_{Pd} [nm]	d_{PdO} [nm]
Paper I							
0.23PdAl	500°C, 2h	0.23	145	93	0.96	1.2	-
0.47PdAl	500°C, 2h	0.47	144	73	1.5	1.5	-
0.93PdAl	500°C, 2h	0.93	146	54	2.3	2.1	-
1.9PdAl	500°C, 2h	1.9	140	34	2.9	3.3	-
3.6PdAl	500°C, 2h	3.6	138	21	3.4	5.3	-
0.47PdAl-TT	800°C, 7h	0.47	134	47	0.99	2.6	-
0.93PdAl-TT	850°C, 3.5h	0.93	129	32	1.3	3.5	-
1.9PdAl-TT	900°C, 4h	1.9	122	14	1.1	8.3	-
3.6PdAl-TT	900°C, 6h	3.6	118	8.5	1.3	13	-
Paper III							
PdO	-		87	13	-	7.2	61	17
Pd/γ-Al$_2$O$_3$-500	500°C, 2h	1.9	140	33	2.9	3.4	-
Pd/γ-Al$_2$O$_3$-900	900°C, 2h	1.9	130	10	0.93	11	18
Paper IV							
Pd/Al$_2$O$_3$	500°C, 1h	5	-	20	-	-	6
Paper V							
Pd/Al$_2$O$_3$-$D_{57\%}$	500°C, 2h	1.7	142	57	4.3	2.0	-
Pd/Al$_2$O$_3$-$D_{14\%}$	900°C, 2h	1.8	131	14	1.1	8.0	18
Pd/ZSM-5-$D_{21\%}$	500°C, 2h	1.8	387	21	1.7	5.4	-
Pd/ZSM-5-$D_{5.2\%}$	500°C, 2h	1.7	368	5.2	0.39	22	37

CHAPTER 3

CATALYTIC METHANE OXIDATION

The strive to develop catalysts with high activity for lean methane oxidation has for several decades motivated trial-and-error approaches for preparation and evaluation of many different catalysts formulations [54–57]. The general consensus among researchers is that for oxygen excess conditions, palladium-based catalysts show the highest catalytic activity for methane oxidation at temperatures below 635 °C because under these conditions, a stable phase of palladium oxide forms that possesses a high catalytic activity [58]. In recent years, compelling evidence about preferred terminations of ideal palladium oxide surfaces with low energy barriers for methane oxidation have been obtained by *in situ* surface sensitive experimental techniques and first-principles calculations [18, 59–61]. As mentioned in the Introduction, dissociative methane adsorption is typically considered to be the rate-determining step for methane oxidation and facets with low energy barriers for this step are hence highly preferred. Over PdO(100), which is the most common termination, the energy barrier is rather high [62–65]. The energy barrier over the second most common termination [62, 66], PdO(101), is however significantly lower and this surface is in fact recognized as the most active palladium oxide facet for methane oxidation [59, 67, 68]. The PdO(101) surface contains palladium and oxygen atoms with threefold coordinations. A lower repulsion is exerted on the methane molecule that approaches a Pd atom having a threefold coordination compared to Pd atoms with higher coordination numbers on other surfaces. This is thanks to the oxygen atom located below the palladium atom for this structure, which depopulates the d_{z^2} orbital that otherwise would repel the molecular orbitals of methane [59]. The facile

methane dissociation on Pd(101) is thus not only connected to the low energy barrier but also to the higher sticking probability of methane. Studies of methane oxidation over ideal surfaces with atomic control bring conclusive results. Identified mechanisms may operate also on supported palladium catalysts, however, comparisons should be made with care. Supported palladium includes, in addition to ideal facets, a plethora of sites on, e.g., connected facets, edges and corners as well as sites on the particle rim in contact with the support. Thereby Pd sites with many different coordinations might be present. The fraction of these (non facet) sites will be higher for small particles and eventually promote the overall reaction rate. Small particles will furthermore have a higher fraction of surface sites close to the particle rim, i.e. metal sites adjacent or in close vicinity to the support. In some catalytic systems, rim sites are believed to have a significant role [69–72]. Strong metal-support interaction is another aspect that may alter the catalytic activity of active sites, due to an electronic influence [73–75]. Theoretical studies on oxidation of carbon monoxide have provided evidence that the interplay between different types of active sites should be considered to understand a more complex reaction landscape [76].

To judge whether or not a catalyst formulation is better than another can be challenging. Reported measured catalytic activities may be influenced by experimental artifacts or obtained at conditions not in full reflecting the intrinsic activity. To compare different catalysts based on conversion data one should normalise the rates. Turnover frequency (TOF) is a normalised reaction rate that is often used in heterogeneous catalysis. The TOF is determined by dividing the total number of converted molecules, here methane, per unit time by the total number of metal surface sites on the catalyst [77]. In doing this all surface sites are assumed to be identical, which is an assumption not free from debate. Still, however, it may be a useful approach to enable at least a more fair, although not perfect, comparison of catalysts than a direct comparison of conversions. In this thesis TOF has been used when comparing methane oxidation reaction rates for samples with different Pd loading, particle size, morphology and type of support material. An example on how TOF is used for catalyst comparison is shown in Figure 3.1. It shows the extinction profiles for alumina supported Pd particles (Pd/γ-Al$_2$O$_3$-500) and a bare PdO powder sample. The methane TOF is significantly higher over the Pd/γ-Al$_2$O$_3$-500 catalyst compared to the bare PdO powder sample at elevated temperatures. The maximum TOF reached at high temperatures in dry conditions (Figure 3.1a) is al-
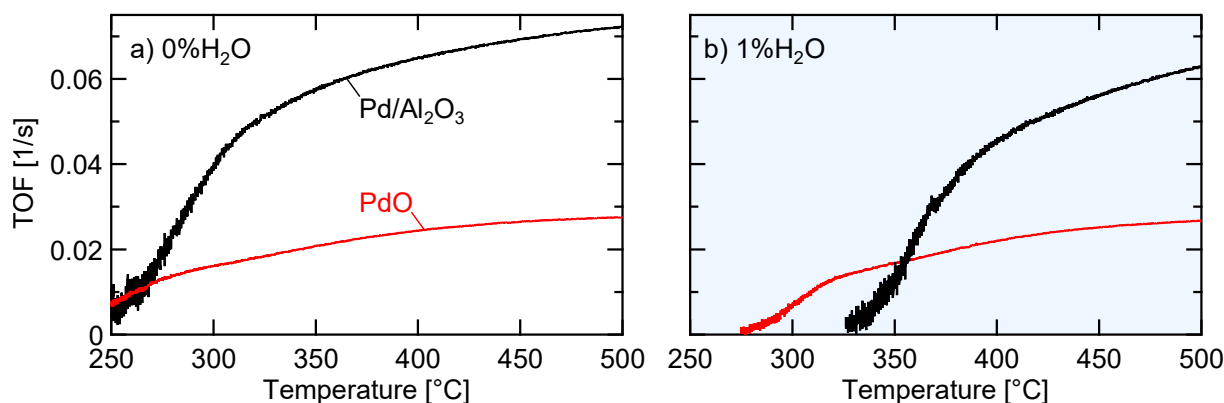
Figure 3.1: Methane turnover frequency over Pd/γ-Al$_2$O$_3$-500 (black) and PdO (red) monolith samples in a) 2% O$_2$ + 0.2% CH$_4$ and b) 2% O$_2$ + 0.2% CH$_4$ + 1% H$_2$O.

most three times higher over Pd/γ-Al$_2$O$_3$-500 compared to PdO where the TOF tends to flatten out on a relatively low level already at 400 °C. A possible explanation to the higher catalytic activity for Pd/γ-Al$_2$O$_3$-500 can be the Pd particle size, where active sites on kinks, edges and corners constitute a larger fraction of the available Pd. For the larger PdO powder grains, a larger fraction of less active sites, for example on facets like PdO(100), can be expected. Furthermore, active sites on rim between the PdO particle and Al$_2$O$_3$ surface may contribute to the higher TOF over the Pd/γ-Al$_2$O$_3$-500 sample. In the presence of water vapor, a slightly different trend in catalytic activity is seen (Figure 3.1b). A higher TOF is observed for the bare PdO powder compared to Pd/γ-Al$_2$O$_3$-500 at temperatures below 350 °C. This indicates that active sites on Pd particles dispersed on a support material like alumina are less tolerant towards water in some conditions. At elevated temperatures however, a significantly higher rate is again observed over the Pd/γ-Al$_2$O$_3$-500 catalyst, although lower than in dry conditions.

3.1 Catalyst evaluation in chemical flow reactor

To examine the catalytic performance of the model catalyst samples, a chemical flow reactor was used. Depending on the form of the catalyst, powder or monolith, different quartz tube reactors were mounted in the reactor setup. For powder samples, a vertical tube with an inner diameter of 4 mm was used wheres a larger one with an inner diameter of 15 mm was used horizontally for monolith samples. For experiments with powder samples, approximately 140 mg of sample was placed between two layers of quartz wool. A thermocouple was positioned in the upstream quartz wool layer close
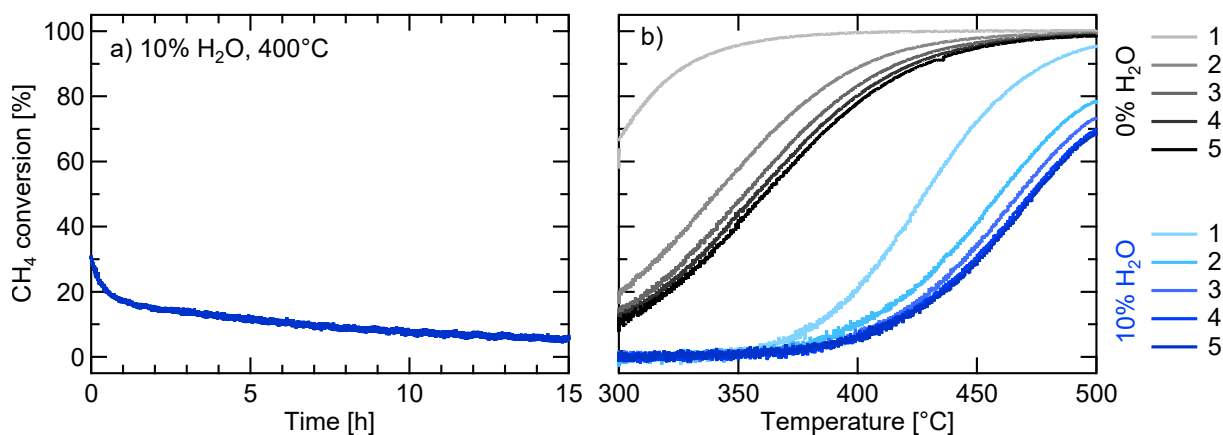
Figure 3.2: a) Methane conversion over a monolith coated with Pd/γ-Al$_2$O$_3$-500 during 15 h exposure to 2% O$_2$ + 0.1% CH$_4$ + 10% H$_2$O at 400 °C. b) Extinction profiles for the same catalyst (initially fresh) in 2% O$_2$ + 0.1% CH$_4$ (black) and 2% O$_2$ + 0.1% CH$_4$ + 10% H$_2$O (blue).

to the sample to monitor the inlet gas temperature. In the experiments with monolith catalysts, an uncoated monolith was placed upstream of the sample and two thermocouples were used. One was placed in the uncoated monolith about 5 mm upstream of the monolith catalyst to measure the inlet gas temperature, which was used for temperature control. The second thermocouple was placed in the middle of the monolith catalyst to measure the catalyst temperature. A metal coil that surrounded the quartz tube was used for resistive heating in both the powder and monolith set-ups. The tubes were insulated by quartz wool to get a more uniform and controlled heating of the catalyst. Feed gas mixtures with CH$_4$, O$_2$, and Ar as carrier gas were introduced to the reactor via mass flow controllers (MFC). Water vapor of different concentrations could be fed to the reactor via a controlled evaporator mixer (CEM) device. The CEM system consists of a controllable heater, a liquid MFC that provides water, and a gas MFC that provides a carrier gas (Ar). The liquid water is vaporized in the furnace and carried to the quartz tube reactor by the Ar flow in tubing heated to 200 °C. A total flow of 200 mL/min was used for the powder measurements, which corresponds to a gas hourly space velocity (GHSV) of 64,000 h^{-1}. For the monolith experiments, a flow of 1200 mL/min was used, which corresponds to a GHSV of 32,000 h^{-1}. The gas feed is assumed to be well mixed and equally distributed through the channels of the monolith samples as well as the powder bed. The effluent gas composition was analyzed by a gas-phase Fourier transform infrared (FTIR) spectrometer.

Prior to catalytic activity tests, the samples were exposed to reaction conditions for

a relatively long time. Figure 3.2a shows that at least 15 h of methane oxidation in wet conditions is required to reach steady state over Pd/γ-Al$_2$O$_3$-500. This procedure can be referred to as catalyst degreening and is important to consider for accurate evaluation of supported noble metal catalysts. Otherwise incorrect conclusions may be drawn from the data. For example an exaggerated emphasis on catalyst formulations with high initial catalytic activity or formulations with higher long-term stability might be overlooked just because its initial catalytic activity is somewhat low, although it might meet performance requirements over time. The extinction profiles in Figure 3.2b show that the ignition-extinction cycle between 300-500 °C needed to be repeated at least four times in both dry and wet methane oxidation conditions as to be reproducible. The total time for this experiment was 26 h and the observed methane conversion in wet conditions at 400 °C correlates well with the degreening procedure displayed in Figure 3.2a.

3.2 Kinetics in dry and wet conditions

The catalytic methane oxidation over both PdO and Pd/Al$_2$O$_3$ is clearly inhibited by water. The remaining part of this chapter will mainly concern the wet methane oxidation kinetics over Pd particles of various size. The performance of both powder and monolith samples was evaluated in the absence and presence of water vapor, which lead to a few general statements.

3.2.1 Methane conversion and product selectivity

Several gas phase components (carbon based) in the reactor effluent stream were monitored to enable mass balance analysis and understand whether or not other compounds than carbon dioxide are formed as methane is converted over Pd/Al$_2$O$_3$ catalysts. Figure 3.3a shows that all methane (1000 ppm) that is fed to the reactor is converted to carbon dioxide in dry conditions and oxygen excess (0-15 min). When oxygen is removed from the feed (15-30 min), a rapid increase in methane concentration is measured in the outlet. The carbon dioxide formation drops to a low level and carbon monoxide instead becomes the main reaction product. Carbon monoxide is a highly unwanted toxic side product and selectivity changes from total to partial oxidation of methane should be avoided. In the presence of water vapor (*cf.* Figure 3.3b), approximately
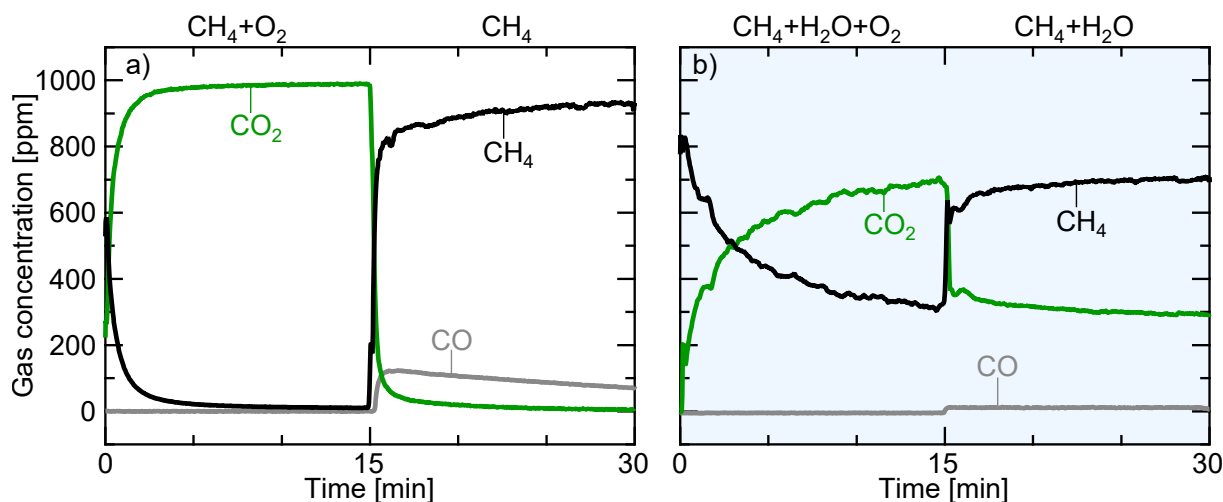
Figure 3.3: Outlet reactor gas concentrations of CH_4 (black), CO (grey) and CO_2 (green) from oxidation of 0.1% CH_4 over Pd/Al_2O_3-57D_{Pd} at 360 °C while periodically turning on/off 1.5% O_2. Panel a shows dry conditions, and panel b in the presence of 1% H_2O.

65% of the fed methane is converted to carbon dioxide over the Pd/Al_2O_3 catalyst, and almost no carbon monoxide is formed. Interestingly, a higher conversion of methane to carbon dioxide is observed in the absence of oxygen in wet conditions compared to dry. This is due to methane steam reforming and the water-gas shift (WGS) reaction where methane first is converted to carbon monoxide that subsequently reacts further with water to form carbon dioxide and hydrogen. In this respect it is thus an advantage to operate methane abatement systems in the presence of water vapor as carbon monoxide during oxygen deficiency periods can be converted to carbon dioxide once the minimum temperature necessary to initiate the WGS reaction (light-off temperature) is exceeded.

3.2.2 Particle size effects

The Pd dispersion and particle size are important design criteria to consider for palladium-alumina based catalysts used in catalytic emission control of methane combustion exhausts. This is discussed in **Paper I**. It has been shown that the shape and size of metal particles dispersed on a support may affect the catalytic performance for many different reactions [78–82]. The remaining part of this chapter will focus on the role of palladium dispersion and particle size for methane oxidation in both dry and wet conditions.

The Pd/γ-Al_2O_3 model catalysts that were prepared to investigate particle size effects can be regarded as two subsets, with denoted sample ID's and physicochemical properties summarized in Table 2.1. The first subset has a targeted Pd loading ranging
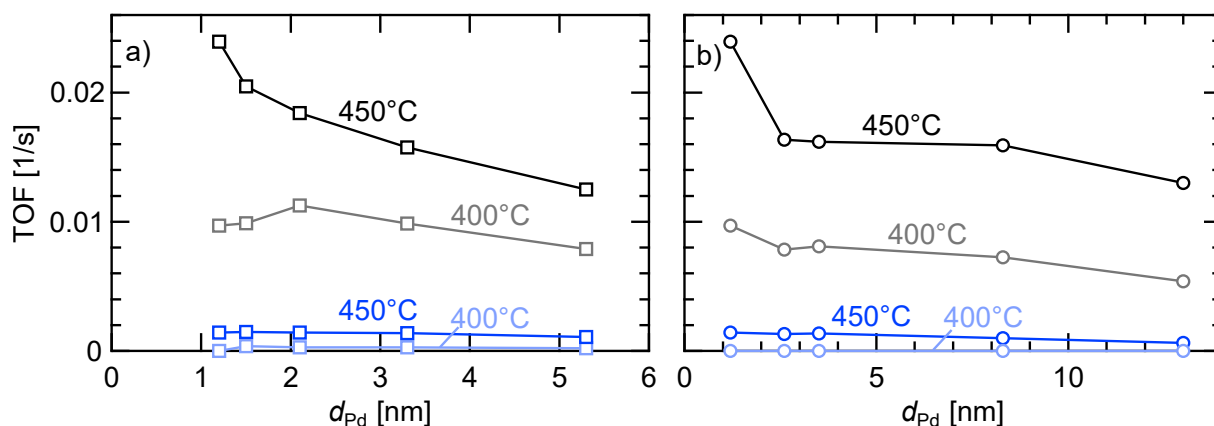
Figure 3.4: Methane turnover frequency *versus* Pd particle size for a) parent and b) thermally treated Pd/Al$_2$O$_3$ powder catalysts at 400 and 450 °C in dry (black lines) and wet (blue lines) conditions.

from 0.25 to 4 wt.-% and is referred to as the parent catalysts. The samples in this subset were calcined in air at 500 °C for 4 h and the palladium surface area increases with increasing Pd loading, as shown in Figure 2.5. The second subset consists of samples where the palladium surface areas are similar to the one with the lowest Pd loading (0.23 wt.%). These samples have gone through a second calcination step in individual harsher conditions where significant Pd particle sintering occurred. This subset is referred to as thermally treated. The fifth extinction profiles for methane oxidation in dry and wet conditions over parent and thermally treated catalysts were gathered. In order to avoid misinterpretations, the kinetic experiments were performed for both powder and monolith samples. From all acquired reactor data, kinetic behaviours and trends were thoroughly examined.

Normalised reaction rate

In Figure 3.4 the methane TOF at 400 and 450 °C is plotted against the Pd particle size for the two sets of powder samples. In panel a, the TOF reaches a maximum value of 0.012 s^{-1} for the sample with a particle diameter of 2.1 nm in dry conditions at 400 °C. At 450 °C, a decreasing TOF is observed over catalysts with larger particles. This is likely due to the high catalytic activity regime reached for all samples where the overall rate to some extent is mass transport limited. In wet conditions, a low TOF is observed at both 400 and 450 °C over all the parent powder samples. For the thermally treated powder samples in Figure 3.4b, the methane TOF decreases with increasing Pd particle size. Since the Pd area is approximately the same for these samples, the high rate

over the sample with smallest particles confirms that an optimum Pd particle size for methane oxidation is obtained somewhere below 3 nm. Samples with a high fraction of small particles have an increasing proportion of edges, corners and rim sites. In wet conditions, the reaction rate is considerably lower also for all thermally treated catalysts. The activity drop, however, is larger for the more highly dispersed catalysts. This indicates that Pd rim sites that possibly promote the reaction rate in dry conditions are less tolerant to water vapor due to more severe blocking by, e.g., hydroxyl groups [83].

Apparent activation energy

To further discuss the effect of Pd particle size on the overall catalytic activity and the occurrence of active rim sites, apparent activation energies (E_a^{app}) were extracted from the methane conversion profiles. According to Figure 3.5a, the (E_a^{app}) of a chemical reaction can be determined from the Arrhenius plot. The natural logarithm of methane conversion during the last extinction processes is plotted against 1/temperature in dry and wet conditions over the 0.23 wt.% Pd/Al_2O_3 catalyst. Linear regression of the slopes in the low methane conversion region ($\leq$ 15%), where the overall rate is kinetically controlled, is then used to obtain the E_a^{app}. One should be aware that the apparent activation energy (E_a^{app}) will differ compared to the activation energy that is determined from the rate constant of a surface reaction. Figure 3.5b displays the apparent activation energies for the thermally treated samples in both dry and wet conditions as a function of Pd particle size. The parent samples are here excluded since the E_a^{app} was determined at different temperatures. This is due to a significant difference in catalytic activity (observed in the extinction profiles in **Paper I**) for these catalysts depending on the Pd loading. The thermally treated samples however exhibited similar extinction profiles and are hence more suitable for E_a^{app} comparisons. The determined values are furthermore in good agreement with those from similar catalytic systems and reaction conditions in literature [26–28, 84–89].

In dry conditions, E_a^{app} increases with increasing Pd particle size for both powder and monolith samples. For monolith catalysts, E_a^{app} is 66 kJ/mol for the catalyst with smallest Pd particles and 99 kJ/mol for the one with the largest particles. The corresponding difference is however not higher than 3 kJ/mol for the powder samples. Due to an additional preparation step for the monolith samples, more error sources may arise from differences in the washcoat layer and decreased Pd availability due to

30
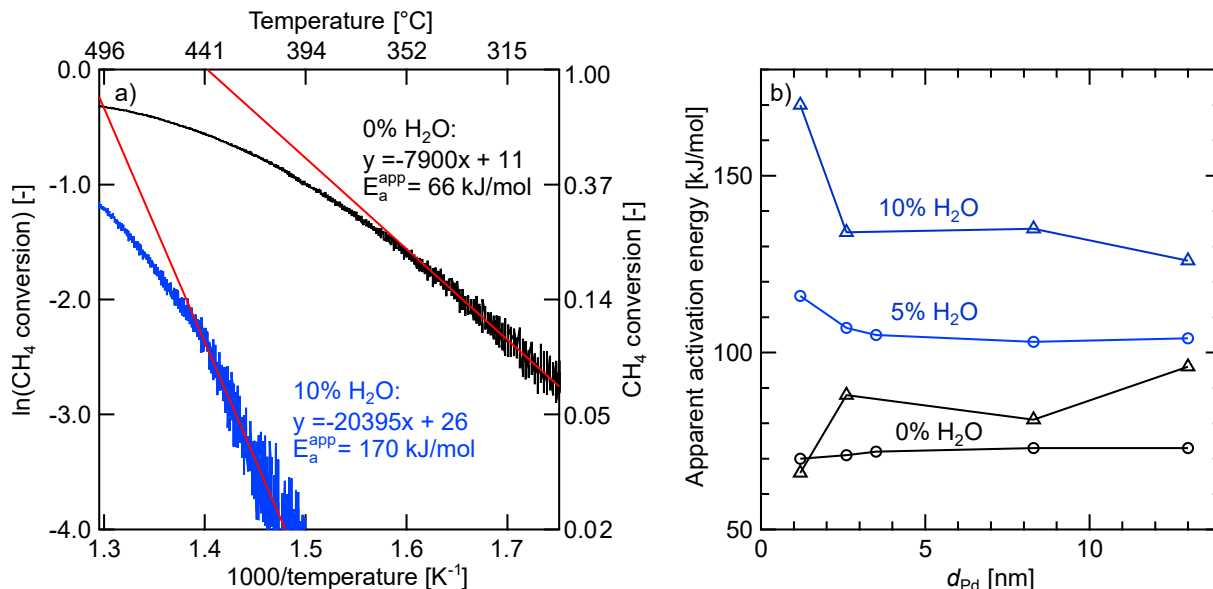
Figure 3.5: a) Arrhenius plots showing the last extinction process in dry (black) and wet (blue) conditions for the 0.23PdAl monolith sample. b) Apparent activation energy for thermally treated Pd/γ-Al$_2$O$_3$ powder ($\circ$) and monolith ($\triangle$) catalysts.

pore blockage and coverage of active sites by the binder material. Differences in space velocity and flow characteristics for the measurements with monolith and powder samples can furthermore give rise to variations in the observed trends. For both powder and monolith samples, considerably higher E_a^{app} are observed in wet conditions in Figure 3.5b. For the powder sample with smallest Pd particles, the E_a^{app} increases from 70 to 116 kJ/mol when water is introduced to the feed. On the contrary to dry conditions, the E_a^{app} decreases with increasing Pd particle size. A similar trend is also observed for the monolith samples. For the monolith experiments a higher water concentration of 10 vol.% was used which increased the E_a^{app}. The observed trends in E_a^{app} support the existence of different active sites, with varying activity for methane oxidation and sensitivity towards water. The fraction of these sites is dependent on the Pd dispersion, which in turn will affect the overall reaction rate. The findings suggests that methane oxidation over catalysts with mainly large Pd particles proceed predominantly on PdO sites without contact with the alumina support. However, sites on the Pd particle rim, corners and edges become more important for highly dispersed Pd catalysts, and contribute to a higher degree to the overall reaction rate. Several studies for different types of catalytic systems have previously reported that these rim sites may improve the reaction rate [70–72, 90–94].

31

MONITORING ADSORBATE SPECIES

4.1 Probing molecules with infrared radiation

Infrared (IR) spectroscopy is a useful method to probe gas-phase reactants and product molecules as well as intermediate and spectator species adsorbed on the surface of the catalyst. The method relies on the interaction of photons in the infrared part of the electromagnetic radiation spectrum with chemical compounds. The interaction occurs at characteristic frequencies when vibrational or rotational modes of a covalent bond match a certain photon energy. This triggers a change in dipole moment of the bond and excites the vibrational mode to a higher energy level [95]. Consequently, the substance in a sample is revealed by the decreased intensity, known as absorption bands, of the transmitted IR radiation at specific frequencies that reaches an infrared detector. In IR spectroscopy, the frequency of an absorption band in the spatial domain is commonly expressed in cm^{-1} by a parameter called wavenumber ($\tilde{\nu}$). The wavenumber position of a vibrational mode is related to the bond strength and atom mass at either end of it. In addition, as a first approximation, the magnitude of the absorbance (A) is related to the concentration (c) of the light-absorbing species according to the well-known Beer-Lambert law [42] as:

$$A = \epsilon b c \tag{4.1}$$

where ϵ is the extinction coefficient and b the sample thickness. The variation in absorbance at different wavenumbers gives rise to an absorption spectrum, which can be used for qualitative and quantitative analysis of the sample depending on the probing
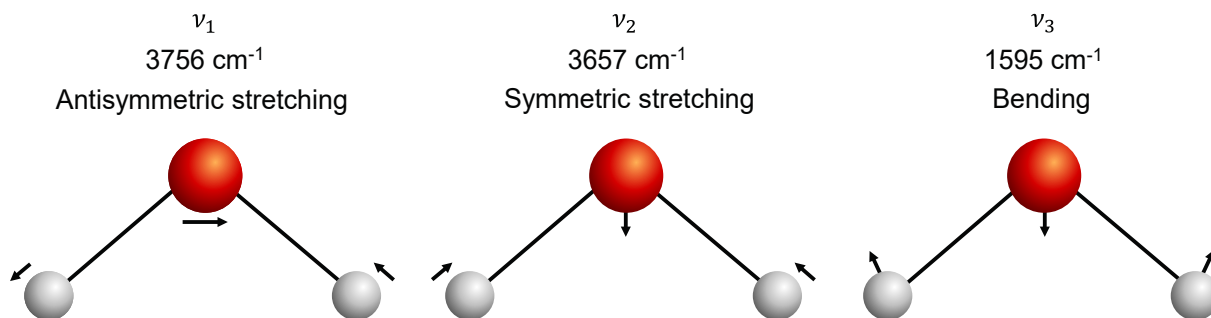
Figure 4.1: Illustration of the vibrational modes of a water molecule.

mode.

In this thesis, the mid-infrared region ranging from 400-4000 cm^{-1}, has been used for qualitative identification of surface-bound species on the examined samples in various reactant mixtures. Molecular assignment of the evolved absorption bands during these measurements requires knowledge about vibrational modes. For isolated multiatomic molecules, the actual vibrational degrees of freedom are dependent on shape and number of atoms (N). The true vibrations of linear molecules are $3N - 5$ and $3N - 6$ in the case of non-linear ones. The product $3N$ corresponds to the three directions in space that each atom can move in, and the subtracted number relates to translational and rotational modes with near zero frequencies. Hence, the remaining modes of a diatomic molecule like carbon monoxide is only one, assigned to symmetric stretching of the C-O bond. Another example of true vibrations is illustrated for the triatomic non-linear water molecule in Figure 4.1. Water has three ($3 \times 3 - 6$) modes of vibrations that all are IR-active and correspond to antisymmetric stretching ($\tilde{\nu}_1$) at 3756 cm^{-1}, symmetric stretching ($\tilde{\nu}_2$) at 3657 cm^{-1} and bending ($\tilde{\nu}_3$) at 1595 cm^{-1} modes [95]. As shown when PdO is exposed to water vapor in section 4.3, gaseous water gives rise to a rich spectrum with several absorption bands. This is due to its small moment of inertia on rotation, causing a large number of combined vibrational-rotational bands to appear.

## 4.2 Modes of infrared spectroscopic characterisation

4.2.1 Fourier transform infrared spectroscopy

The wide use of infrared spectroscopy is owing to the rich chemical information that can be obtained, and several thorough descriptions of a variety of applications are available

in the literature. Fourier transform infrared (FTIR) spectroscopy has for decades been recognised as one of the most important IR analysis methods as it offers high signal-to-noise ratio, acquisition speed and frequency accuracy. In the FTIR spectrometer, the so-called interferometer plays a crucial role. A simplified schematic of the classical Michelson interferometer is illustrated in the top left part of Figure 4.2. Briefly, a semi-transparent mirror (beam splitter) splits the IR radiation coming from the source. Approximately half of the intensity of the light is transmitted towards a movable mirror and the other fraction is directed to a fixed mirror. The beams are then reflected by the mirrors back to the beam splitter and recombine. Some of the recombined (modulated) radiation travels back towards the IR source and is lost while the remaining part can be used for sample analysis as it is directed towards the sample and detector. Differences in optical path length for the beams lead to constructive and destructive interference of the recombined beams and an amplitude that is either reinforced or cancelled out. For intermediate phase differences, partial cancellation takes place [95]. The collected raw data is called an interferogram and displays the relative intensity as a function of position of the moving mirror. Finally, the spectral raw data is mathematically converted to the frequency (wavenumber) domain by Fourier transform. All in all, the construction enables that an entire spectrum, ranging over a wide span of wavenumbers, rapidly can be observed at once [42].

4.2.2 *Operando* diffuse reflectance infrared spectroscopy measurements

There are generally a few modes whereby samples can be irradiated with modulated IR radiation for FTIR spectroscopic studies. Aside from measurements in transmission mode, several reflection methods have been developed in recent years. In all, the reflection methods can be categorized in three classes known as specular reflectance, attenuated total reflectance and diffuse reflectance [95]. In this thesis, *operando* characterisation of surface-bound species has been carried out by infrared Fourier transform spectroscopy in diffuse reflectance mode, known as DRIFTS. Figure 4.2 shows a schematic of the used DRIFTS setup. Modulated IR radiation is directed towards the powder sample by an ellipsoidal mirror. Upon hitting the sample it scatters within the sample (the scattering is limited by the penetration depth), interacts with the sample
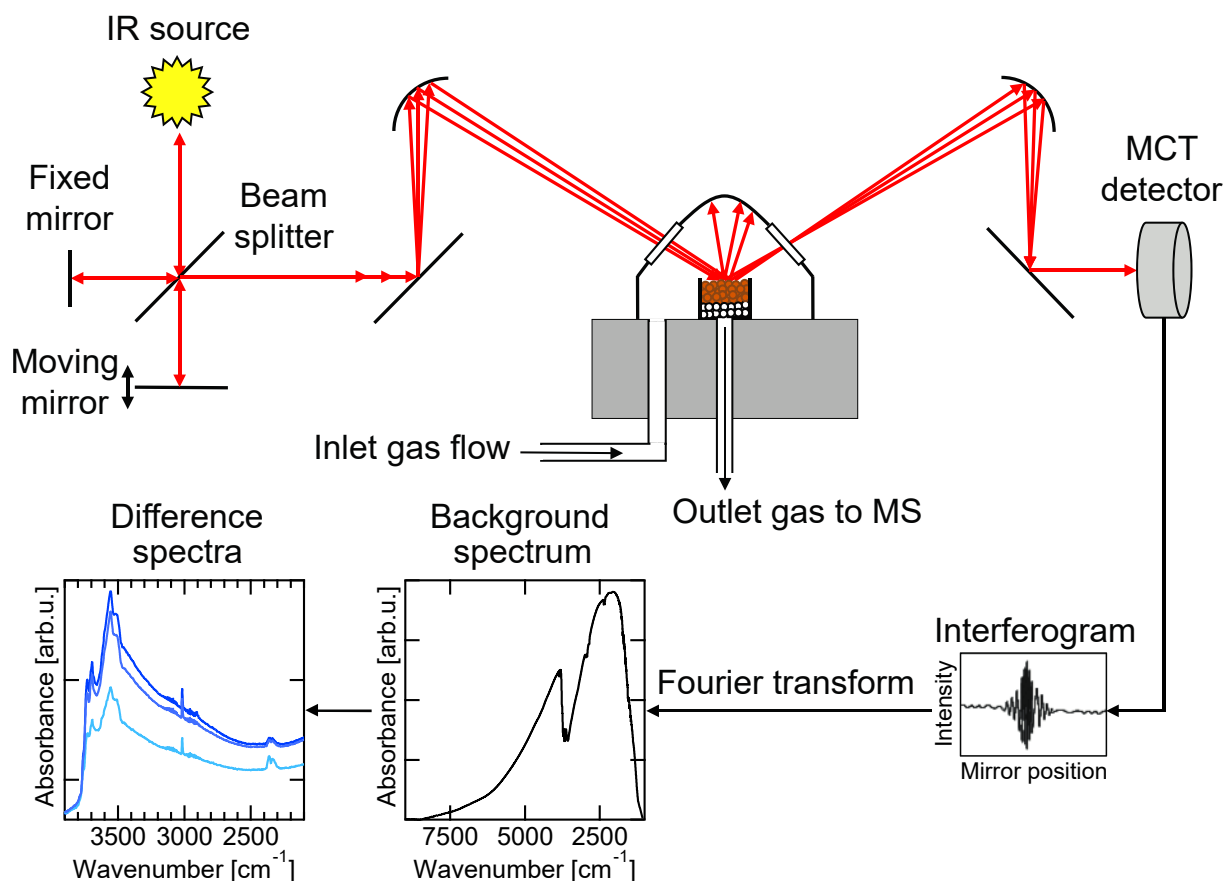
Figure 4.2: Schematic of diffuse reflectance infrared Fourier transform spectroscopy setup.

and is reflected in a diffuse manner in multiple angles. The reflected radiation is then collected by a second ellipsoidal mirror and directed towards the detector [96].

The DRIFTS technique is relatively simple to use as minimal sample preparation often only including sieving to a homogeneous powder mixture of appropriate particle size and possibly mix with some diluent. The diluent should be an optically transparent powder, like potassium bromide, that in case of a poor signal can be used to increase the reflectivity from the sample volume. A drawback is the lack of linear relationship between IR absorption and concentration of absorbing species. Hence, quantitative analysis is complicated and commonly neglected. Instead, dynamic trends in the absorbance of different surface-bound species is examined and possibly related to kinetic measurements.

Informative *operando* studies require not only that meaningful spectroscopic information is collected but also reliable kinetic data. For this it is important to have an appropriate reaction cell, a fast and clean gas supply, relevant product analytics etc. In order to avoid sampling and collection of flawed data, one should be aware of potential

pitfalls. Concerning catalytic studies, powder samples enable a large catalyst surface area to be exposed to the fluid phase, which governs transport of reactants/products to/from the active sites [97]. The large dead volume, however, often encountered in commercial reaction cells may pose some artifacts. It could lead to misinterpretation of data since the sampling time resolution becomes faster than the actual gas exchange [98]. To alleviate this problem one can for example increase the total flow rate or design a new cell with minimized internal volume. Another issue revealed by Meunier et al. is the significant deviation of effective bulk and surface temperatures of the catalyst bed compared to the set-point temperature measured by a thermocouple located below the sample bed [99]. In our infrared spectroscopy measurements, an additional thermocouple was placed in the sample bed close to the radiated surface to ensure that spectra could be correlated with the correct temperatures. Another matter to bare in mind is that the reaction cell dimensions rarely are optimized for kinetic measurements, i.e., fulfilling that the length-to-diameter ratio of the sample bed length is sufficiently high.

Reliable spectroscopic studies of the effect of water were carried out with a portable water vapor generator device, illustrated in Figure 4.3a and thoroughly described in **Paper II**, connected to the system. As shown in Figure 4.3b, an accurate and precise supply of ultra-pure water vapor over a range of low volume concentrations is possible. The water is produced by catalytic hydrogen oxidation over a 10 wt.% Pt/SiO_2 catalyst heated to 300 °C. Male connectors welded to the inlet and outlet sections make installation on various systems fast and durable. The small and robust design of the device improves its lifetime and facilitates transportation to other research facilities.
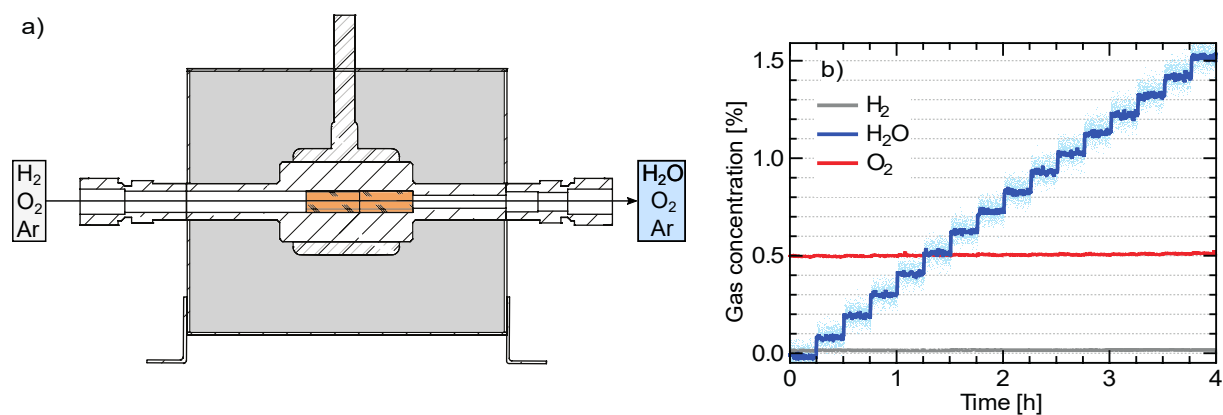
Figure 4.3: a) Schematic drawings of the portable water vapor generator device. b) Generation of 0-1.5% H_2O (g) in 0.5% O_2 excess with Ar balance.

37

4.3 Evolution of adsorbate species during CO chemisorption and methane oxidation

The characterisation of the type of surface species and their evolution on the catalysts during CO chemisorption and methane oxidation conditions is central in this thesis and examined in **Paper I** and **Paper III**. Upon CO chemisorption, the formation of surface-bound carbonyls with different configurations on reduced palladium is studied as to learn about the presence of different sites and their proportions, which is used for determining the relevant stoichiometric factor and active surface area for each catalyst. Further, the formation and stability of surface hydroxyl species are investigated for several catalysts using systematically varied reaction conditions as to understand the mechanisms behind the water inhibition in catalytic methane oxidation.

Surface carbonyls

As described in section 2.2.3, CO uptake measurement is a sensitive method for determining the number of palladium surface atoms of the catalysts provided that the CO adsorption configurations are sufficiently well known. Figure 4.4a shows that a variety of carbonyl configurations, attributed to linear and bridge-bonded species, are adsorbed on the catalysts with different palladium loadings (**Paper I**). The magnitude of the carbonyl bands increases with increased palladium loading as summarized in Table 2.1. The most characteristic difference in spectral shape involves the bridge-bonded absorption band at 1990 cm^{-1} that becomes significantly more intense for catalysts with higher palladium loading. To distinguish the carbonyl configurations and estimate their relative proportions, Voigt profiles as shown in Figure 4.4b were used to deconvolute the absorption bands. The deconvolution procedure is explained in more detail in **Paper III**. By integration of the fitted absorption bands for linear (2084, 2062, and 2047 cm^{-1}), bridge (1989, 1948, 1904 cm^{-1}), and 3-fold hollow (1811 cm^{-1}) bonded CO, a comparison of the proportions of the different carbonyl species for the different samples can be made [49–51]. Assuming negligible differences in extinction coefficients, the obtained proportions were used to determine the stoichiometric factors (F_S) for CO adsorption on Pd atoms [100]. A predominant amount of bridge-bonded CO species is shown for all samples, giving rise to F_S of 2.1-2.2 Pd atoms per adsorbed CO molecule.

A similar type of CO adsorption measurement was performed for γ-Al$_2$O$_3$ and Pd/γ-
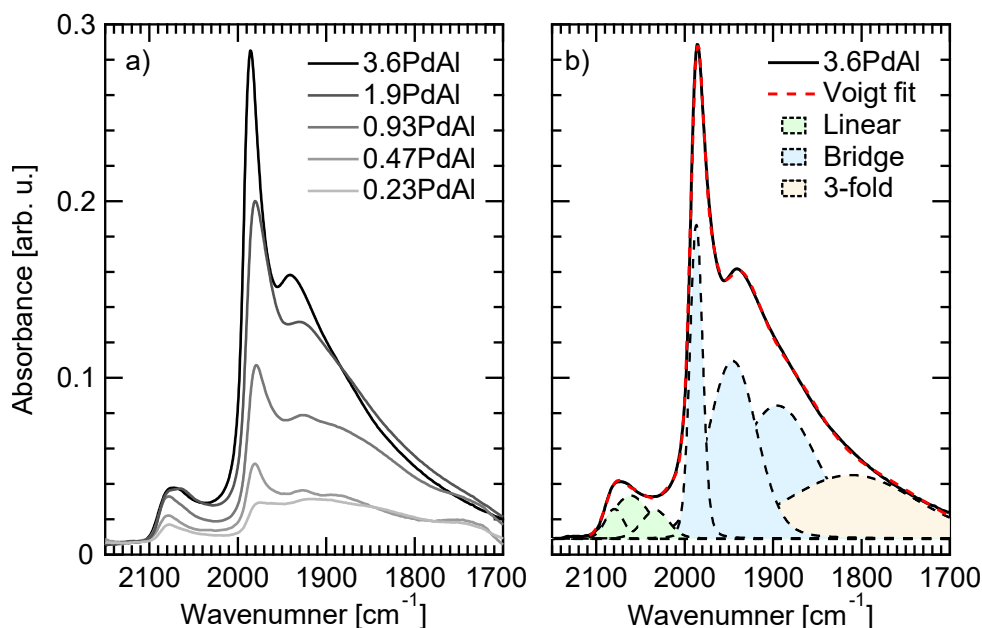
Figure 4.4: a) Difference infrared spectra for Pd/Al$_2$O$_3$ catalysts with different Pd loading recorded in Ar at 35 °C 20 min after exposure to 0.2 vol.% CO for 20 min. b) Difference spectrum for the 3.6PdAl sample and the deconvolution into different CO adsorption configurations.

Al$_2$O$_3$ catalysts calcined at different temperatures as described in **Paper III**. In addition to dry conditions, the measurements were carried out in the presence of 1% water vapor. Under those conditions, a lower coverage of carbonyls is observed as a decreased IR absorbance. Further, some carbonyl bands shift to lower wavenumbers, which indicates interactions with hydroxyls adsorbed on Pd [51, 101–103]. Thus, the altered spectral shape can be interpreted as water or hydroxyl species are adsorbed on palladium.

Surface hydroxyls

It has been proposed that hydroxyl species on Pd/Al$_2$O$_3$ catalysts inhibits the catalytic activity for methane oxidation by blocking active sites [29, 104–107]. Figure 4.5a illustrates the different surface hydroxyl configurations that were examined in **Paper III** and assigned according to experimental and theoretical studies [108–113]. The remaining panels of Figure 4.5 show IR absorption spectra acquired for PdO, γ-Al$_2$O$_3$, Pd/γ-Al$_2$O$_3$-500, and Pd/γ-Al$_2$O$_3$-900 in different mixtures of oxygen, methane and water.

For unsupported PdO, the IR absorption bands at 1300 and 3000 cm^{-1} observed in the black spectrum during dry CH$_4$ oxidation in Figure 4.5b, correspond to gas phase methane, and the smaller band at 2350 cm^{-1} corresponds to gaseous CO$_2$. Upon adding water to the feed, multiple IR absorption bands due to water appear in the lower blue
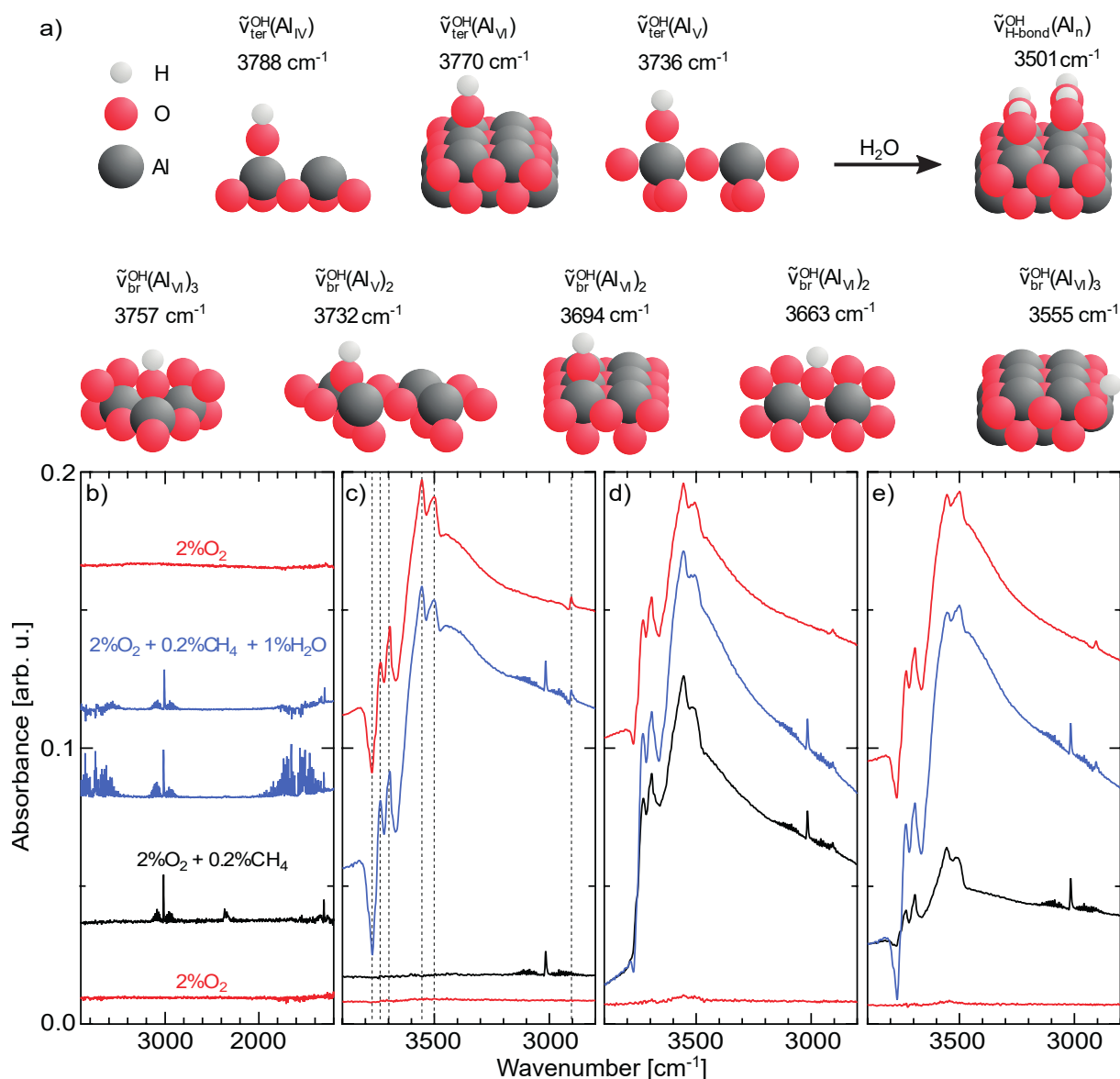
Figure 4.5: a) Schematic representation of hydroxyl species on alumina proposed in the literature and observed in this thesis. IR absorption difference spectra recorded at 280 °C (reference spectrum in O_2) over b) unsupported PdO, c) γ-Al_2O_3, and Pd/γ-Al_2O_3 catalysts calcined at d) 500 °C, and e) 900 °C.

spectrum. In the upper blue spectrum, these bands have been removed using a water compensation tool in the OPUS software (used for all spectra shown hereafter) in an attempt to isolate hydroxyl stretching modes possibly adsorbed on PdO. Despite compensating for water, no absorption bands for (surface) hydroxyls are observed. The lack of evidence should however not be considered as a proof of non-existence. The specific surface area and reflectivity of the nearly black PdO powder sample might be too low to allow detection even in the case of high hydroxyl coverage.

Figure 4.5c shows that addition of 1.0 vol.% H_2O to the reactant feed gives rise to one negative and four positive absorption bands for the γ-Al_2O_3 sample. The negative band with its minimum at 3770 cm^{-1} corresponds to suppression of a linear hydroxyls ($\tilde{\nu}_{ter}^{OH}(Al_{VI})$) that still was present on the alumina surface after pretreatment when the reference spectrum was recorded. During increased coverage of linear hydroxyls, the negative IR absorbance becomes more pronounced and a perturbed vibrational band ($\tilde{\nu}_{H-bond}^{OH}(Al_n)$) evolves at 3501 cm^{-1}. The three remaining bands seen in the blue difference spectrum at 3736, 3694 and 3555 cm^{-1} are attributed to $\tilde{\nu}_{ter}^{OH}(Al_V)$, $\tilde{\nu}_{br}^{OH}(Al_{VI})_2$ and $\tilde{\nu}_{br}^{OH}(Al_{VI})_3$, respectively. The top red spectrum recorded in the end of the experiment after 20 minutes of oxygen treatment reveals that the accumulated hydroxyls on the surface are rather stable and require higher temperatures to be decomposed.

Similar difference spectra are seen for the Pd/γ-Al_2O_3 catalysts in the presence of water vapor in Figure 4.5d and e. However, an extensive build-up of hydroxyl species is already seen during dry methane oxidation conditions as a consequence of product water. The hydroxyl formation from the reaction differs between the two catalysts and a higher absorption is correlated to a higher active metal dispersion. Addition of water to the reactant mixture shows that the hydroxyls formed in the reaction are not sufficient to saturate the extended alumina surface. In wet conditions, the main spectral difference between the two catalysts concerns the perturbation of linear hydroxyls. For Pd/γ-Al_2O_3-500, a minor negative band at 3770 cm^{-1} reveals a low abundance of linear hydroxyls that can be suppressed by water addition. This correlates to the perturbed band at 3501 cm^{-1} that appears as a shoulder and not a pronounced peak as observed for γ-Al_2O_3 and Pd/γ-Al_2O_3-900. This indicates that the concerned sites are blocked by well dispersed Pd as a result of the impregnation and mild calcination [114].

To delve deeper into the formation routes of surface hydroxyl species, a modified experimental procedure was used to study the Pd/γ-Al_2O_3-500 catalyst. The blue difference spectra in Figure 4.6a and b show a rapid evolution of surface hydroxyl groups through dissociation of water vapor at both 280 and 350 °C, which ceases relatively fast. As expected, the largest hydroxyl build-up is observed at the lower temperature due to a lower rate of desorption. After 15 min of oxygen/water exposure, new reference spectra were recorded, and methane was subsequently added to the feed. A further considerable hydroxyl build-up is then seen despite the significantly lower amount of water formed by the reaction than provided by the water vapor generator device.
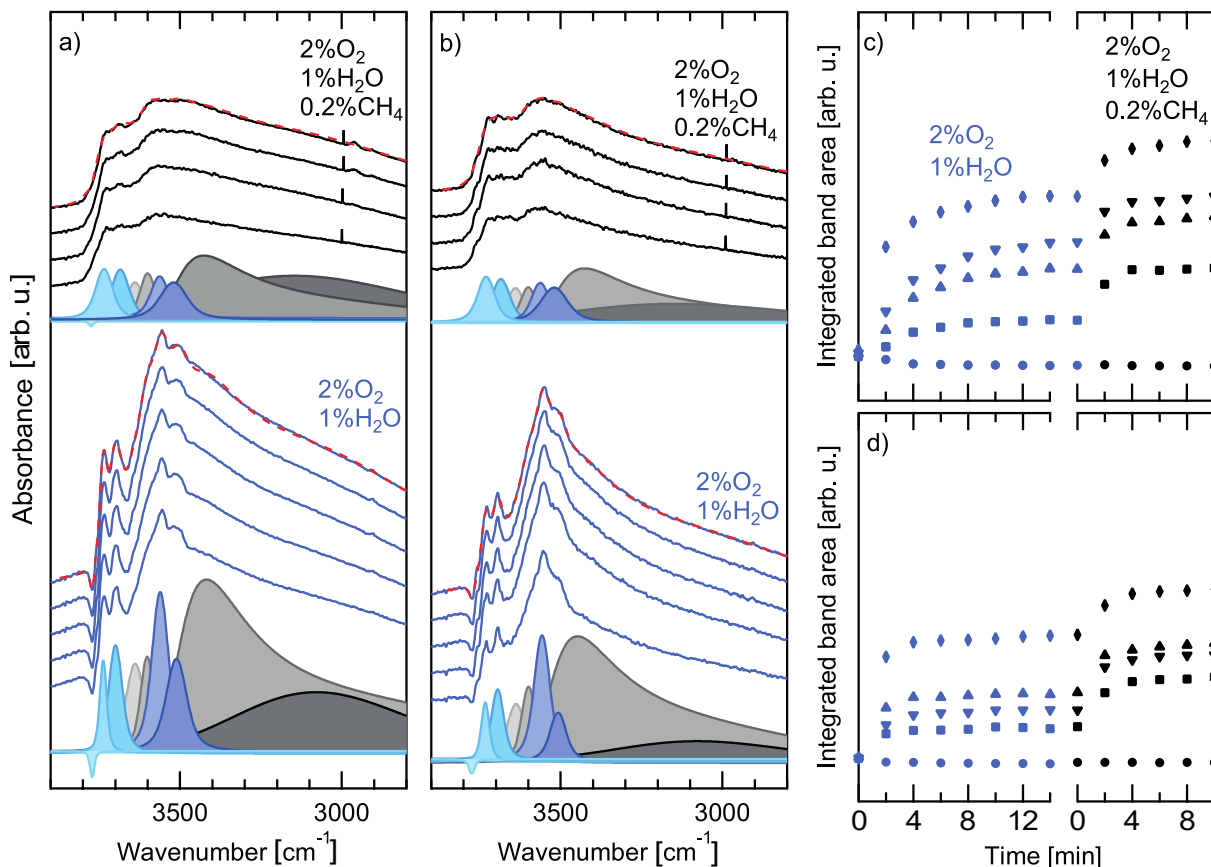
Figure 4.6: Difference spectra recorded in O_2 + H_2O over Pd/γ-Al$_2$O$_3$-500 (O_2 reference spectrum) until steady state where a new reference spectrum was recorded before CH_4 addition at a) 280 °C and b) 350 °C. Hydroxyl build-up is monitored at c) 280 °C and d) 350 °C for the $\widetilde{\nu}_{ter}^{OH}$(Al$_{VI}$) (○), $\widetilde{\nu}_{br}^{OH}$(Al$_V$) (□), $\widetilde{\nu}_{br}^{OH}$(Al$_{VI}$)$_2$ (△), $\widetilde{\nu}_{br}^{OH}$(Al$_{VI}$)$_3$ (◇) and $\widetilde{\nu}_{H-bond}^{OH}$(Al$_n$) (▽) absorption bands.

To better track dynamic changes in hydroxyl coverage, each difference spectrum was deconvoluted by curve fitting using Voigt profiles. As displayed in Figure 4.6c and d, an instantaneous response is seen for all integrated absorption bands that were monitored when first water and then methane was added to the inlet gas mixture. The integrated band area for hydroxyls evolved during the initial water step is clearly lower for the experiment carried out at 350 °C. The hydroxyl build-up generated by methane oxidation in the second step is approximately the same for the two temperatures. This is due to a significantly higher catalytic activity for methane oxidation at 350 °C and hence a higher hydroxyl formation. The increase in hydroxyl coverage at 350 °C compared to 280 °C is, however, limited by a higher desorption rate. Although no distinct differences are seen for the hydroxyls formed by the two routes, it is clear that methane oxidation provides an additional formation path. Provided by supporting experiments

in **Paper III**, we suggest that one such plausible path is spill-over of hydrogen reaction intermediates to alumina sites in the close proximity of the PdO particles.

In addition to the instantaneous decrease in catalytic activity and rapid hydroxyl build-up caused by water, a long term-effect was seen in section 3.1. This effect conforms with previous studies [29, 115, 116], and is here investigated by a 24 h *operando* DRIFTS-MS methane oxidation experiment in dry and wet conditions over Pd/γ-Al$_2$O$_3$-500, see Figure 4.7. The deconvoluted band areas in the top panels show an increased hydroxyl coverage over time that correlates with a declined catalytic activity as shown in the bottom panels. In the absence of water, the experimental time was not sufficient to reach steady state. Hence, the continuous hydroxyl accumulation observed during the first and final 5 h of the experiment, has a negative impact on the reaction kinetics at 330 °C. The hydroxyl build-up is even more pronounced in wet conditions where the catalytic activity decreases faster and reaches zero level after 5 h. Palladium area mea-
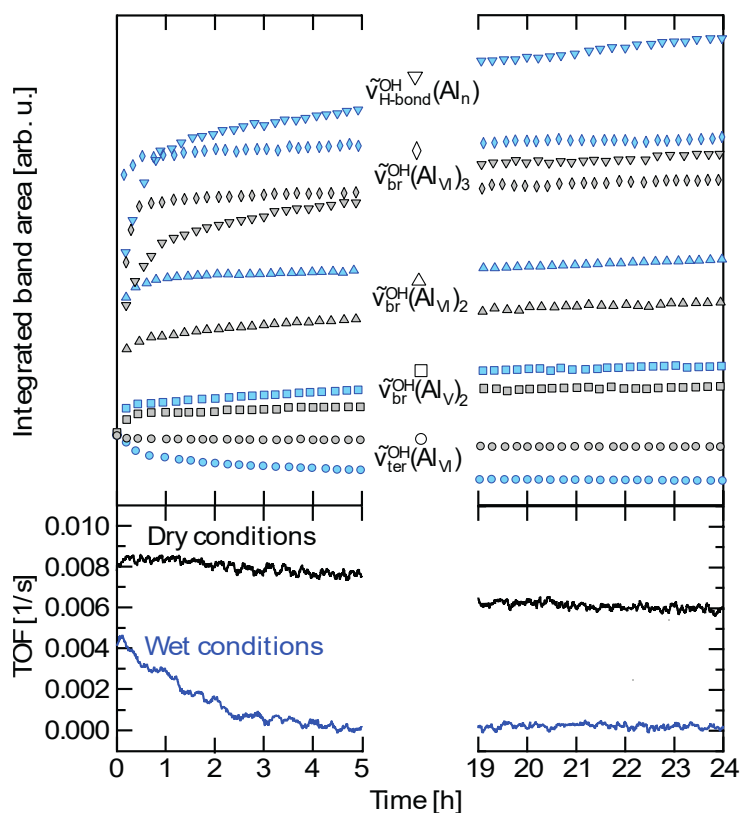
Figure 4.7: 24 h exposure of Pd/γ-Al$_2$O$_3$-500 to dry (black) and wet (blue) methane oxidation conditions at 330 °C. Hydroxyl build-up is monitored in the top panel for the $\widetilde{\nu}_{ter}^{OH}$(Al$_{VI}$) (○), $\widetilde{\nu}_{br}^{OH}$(Al$_V$)$_2$ (□), $\widetilde{\nu}_{br}^{OH}$(Al$_{VI}$)$_2$ (△), $\widetilde{\nu}_{br}^{OH}$(Al$_{VI}$)$_3$ (◇) and $\widetilde{\nu}_{H-bond}^{OH}$(Al$_n$) (▽) absorption bands. Catalytic activity is monitored as methane TOF in the bottom panel.
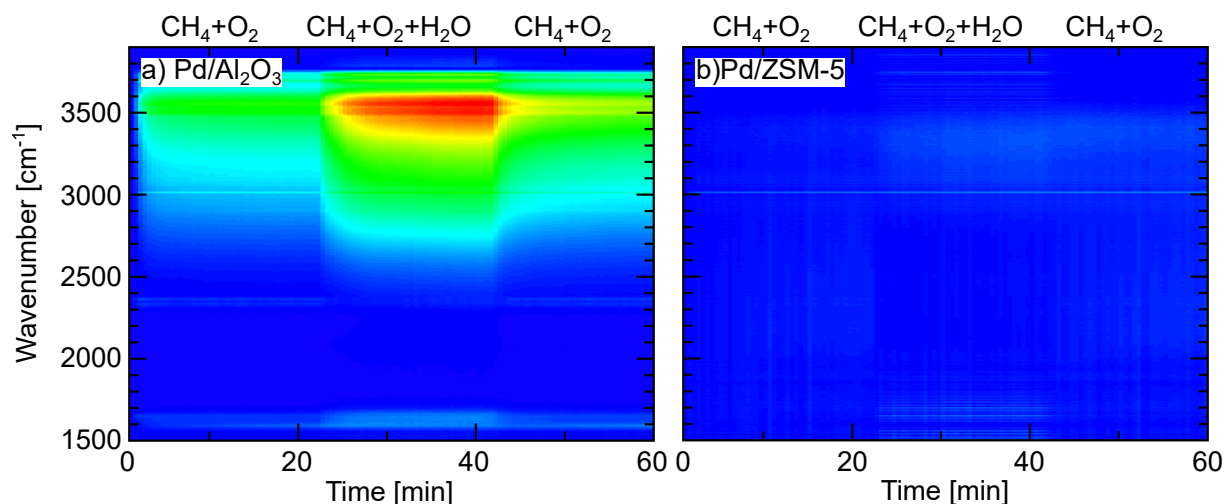
Figure 4.8: Color coded intensities (red corresponds to high and blue low intensity) of IR absorption bands *versus* time during methane oxidation (0.1% CH_4 + 2% O_2) in 0% H_2O (0-20 min), 2% H_2O (20-40 min), and 0% H_2O (40-60 min) over a) Pd/Al_2O_3-57D_{Pd} and b) Pd/ZSM-5-21D_{Pd} at 300 °C.

surements for the exposed Pd/γ-Al_2O_3-500 powder sample after the long-term exposure reveal no sintering. This is in line with the measurements for degreened monolith samples in section 2.3.3, and reasonable as the catalyst already has been exposed to higher temperatures during the preparation. Regeneration of catalytic activity has been proven possible by thermal treatment in dry conditions. These tests strengthen the idea that the primary effect of water inhibition is due to a high coverage of hydroxyl groups on the alumina surface surrounding the PdO particles. One way to avoid or at least decrease the inhibiting effect of water would therefore be to use another, hydrophobic, support.

Zeolite supported Pd-based catalysts have shown promising results for methane oxidation in the presence of steam [117–120]. To circumvent the inhibiting effect of water and high accumulation of hydroxyls on Pd/Al_2O_3, several catalysts with different zeolite support were prepared and examined. When comparing the evaluated support materials, the catalyst with a ZSM-5 type of zeolite structure and a SAR of approximately 2000 exhibited the highest catalytic activity in wet conditions. As shown in Figure 4.8b, this can be correlated to a negligible build-up of hydroxyl species in both dry and wet conditions on this sample. For the same type of experiment, Figure 4.8a reveals a high hydroxyl formation from both methane oxidation itself (0-20 min) and water dissociation (20-40 min) for an Al_2O_3 supported catalyst. A slight decrease in hydroxyl coverage is then observed in the last step (40-60 min) when water is removed from the feed, although still higher than in the initial dry step.

MONITORING THE STATE OF PALLADIUM

5.1 Probing matter with X-ray radiation

X-rays can be used for bulk material analysis for example of chemical composition as with XRF (section 2.2.1) and long-range order of crystalline structures as with XRD (section 2.2.5). X-ray photoelectron spectroscopy (XPS) is another widespread method with particular relevance for heterogeneous catalysis as it is surface-sensitive and measures elemental composition and chemical states of the elements approximately 0-10 nm into the sample. The XPS measurements, however, are normally performed in ultra-high vacuum to probe the number and kinetic energy of the excited photoelectrons [121]. In this thesis X-ray absorption spectroscopy (XAS) was instead used to study the chemistry of the palladium phase in the catalysts. XAS is a powerful technique that can be used to study both the chemical state and local structure of a given element without the need for long-range order and high vacuum [122]. The technique relies on the ability of core-shell electrons to absorb X-rays of definite energies [123]. The wavelength of the X-rays used for XAS measurements is of high energy, comparable to interatomic distances of 0.10-0.01 nm. A high brilliance of the radiation is required to enable measurements with high spatial resolution. Brilliance, also known as brightness, is basically a measure of X-ray beam intensity and is commonly referred to as number of photons of a given wavelength and direction on a spot per second [124]. To meet this requirement, XAS measurements are primarily performed at synchrotron light sources where the brilliance is up to a hundred billion times higher compared to laboratory X-ray tubes.

In Figure 5.1c typical X-ray absorption spectra are shown. The sharp increase in X-ray absorption, known as an absorption edge, occurs when the photon energy is high enough to excite core-shell electrons in the radiated material. The energy region at high energies above the absorption edge is the so-called *extended X-ray absorption fine structure* (EXAFS) region. Analysis of the EXAFS region can provide information about the local environment of an atom, e.g., coordination number and distance to neighboring atoms. The energy region at around the absorption edge is known as the *X-ray absorption near-edge structure* (XANES) region. Spectral features of the XANES spectra for a specific element are primarily affected by the presence of unoccupied states that can accept the photoelectrons. Comparison of measured spectra with empirical standards can consequently be used to determine the oxidation state of an element.

5.2 Energy-dispersive X-ray absorption spectroscopy

The state of palladium was probed by XAS measurements over the so-called Pd K-edge where photons with energy high enough to excite electrons in the Pd 1s orbital into the continuum is used. The Pd K-edge occurs at approximately 24350 eV, which is covered by the studied region ranging from 23500 to 26500 eV. All *operando* XAS experiments were performed using the energy-dispersive (ED-XAS) technique at beamline ID24 at the European Synchrotron Radiation Facility (ESRF) in France. Figure 5.1a schematically shows the experimental setup. Briefly, a beam of high-brilliance X-rays is focused towards a polychromator crystal by mirrors. The polychromator crystal allows for time resolved measurements by dispersing the radiation into its different frequencies. The dispersed X-rays are focused through the sample and the transmitted radiation is measured by a position-sensitive detector [125]. As indicated in Figure 5.1a, X-rays of high energy (purple) and low energy (red) are recorded on opposite sides of the detector, which give rise an absorption spectrum. For ED-XAS measurements, the time it takes to read out the detected radiation limits the time resolution. Since the read out only takes a few milliseconds, a standard time resolution of 500 ms per spectrum was readily obtained. This is significantly faster than the total gas-exchange time (3 s) in the reaction cell, which still is designed to have a low dead volume [126]. Figure 5.1b shows a color-coded intensity map for a transient ED-XAS experiment with normalised XAS spectra as a function of time. The Pd/Al_2O_3-$D_{57\%}$ catalyst is here studied during periodic oxidation
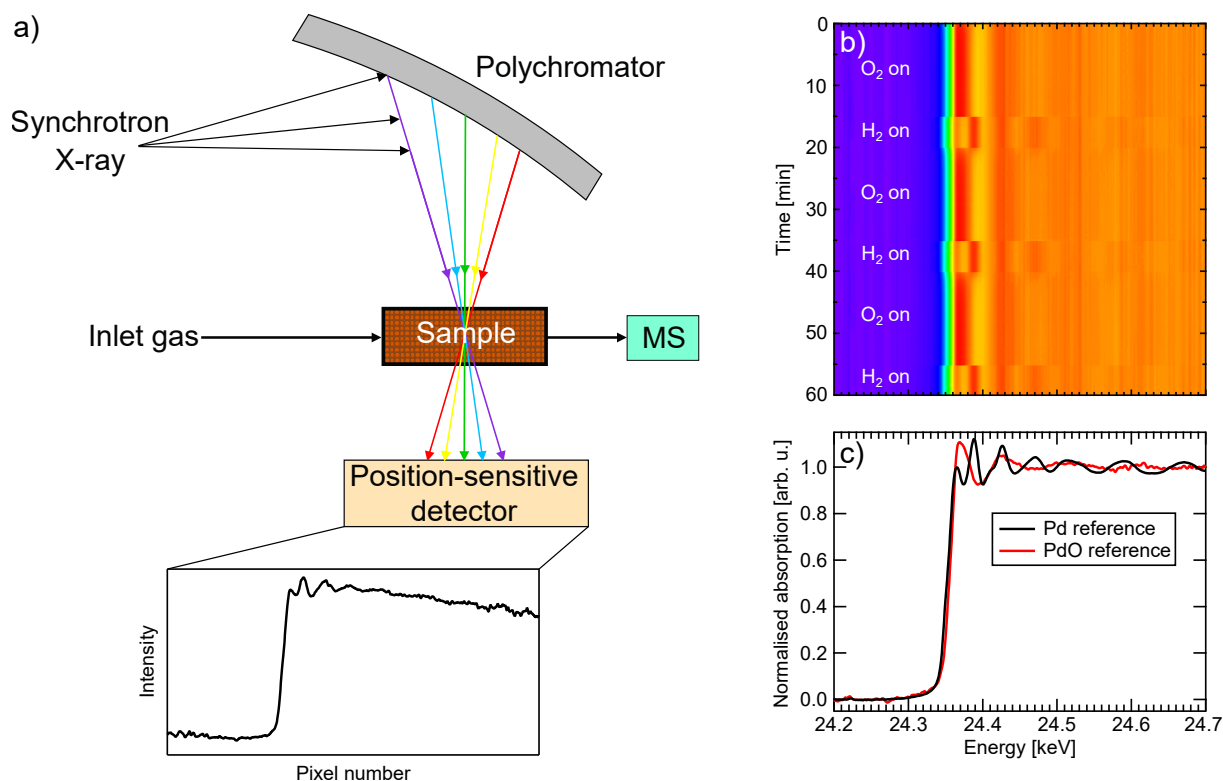
Figure 5.1: a) Schematic of an energy-dispersive XAS setup for *operando* studies. b) Color-coded intensities of XAS spectra (blue corresponds to low intensity and red high) during 15 min oxidising (1.5% O_2) and 5 min reducing (1.5% H_2) periods over Pd/Al$_2$O$_3$-$D_{57\%}$ at 360 °C. c) XAS spectra of palladium foil (black) and oxidised Pd/Al$_2$O$_3$-$D_{57\%}$ (red).

and reduction at 360 °C, starting with a 15 min pulse of oxygen, followed by a 5 min pulse of hydrogen. The sequence is repeated twice, giving rise to a total experimental duration of 60 min. It is clear that the composition of the reactant mixture affects the recorded XAS spectra, and hence the oxidation state of palladium. The observed change is both rapid and reversible. The reversibility is confirmed by the high spectral similarities seen independently of sequential oxidation or reduction period. Further, the spectra recorded at the end of the oxidation and reduction periods are similar to the spectra of Pd foil and PdO powder, respectively. This is thanks to the highly dispersed palladium particles that easily are oxidised and reduced at this temperature. In **Paper IV** and **Paper V**, linear combination fitting of the normalised spectra to known Pd and PdO reference spectra, shown in Figure 5.1c, was implemented to estimate the palladium oxidation state in different conditions [127]. The palladium oxide reference spectrum is here slightly shifted to higher energies and has a significantly larger peak close to the absorption edge compared to the reference spectrum of the metallic palladium foil.

47

5.3 State of palladium during methane oxidation

The structure of a catalyst depends not only on preparation methods but also on the reaction conditions in which it operates. In turn, the catalyst structure determines its function, i.e, catalytic activity and selectivity. This is often referred to as catalyst structure-function relationships, which can be experimentally revealed only by use of *operando* methods. This section presents results from **Paper IV** where the effect of reaction temperature and oxygen concentration on the palladium oxidation state of a 5 wt.% Pd/Al_2O_3 catalyst is correlated to its catalytic performance. Results for a 2 wt.% Pd/Al_2O_3 catalyst from **Paper V** are also presented and compared to experiments performed in the presence of water. Finally, the influence of catalyst formulation in terms of support material and palladium particle size, based on results from **Paper V**, is discussed.

5.3.1 Influence of reaction conditions

The effects of temperature and oxygen concentration on the oxidation state of palladium and its activity for methane oxidation were studied by operando XAS during oxygen step-response experiments in **Paper IV**. Figure 5.2 shows a rapid increase in methane conversion and Pd^{2+} fraction when the feed gas composition is switched from a reducing flow of only methane to a net-oxidizing mixture containing also 0.6, 1.2 or 2.5% oxygen. The high catalytic activity observed immediately after the oxygen pulse is assigned to methane oxidation over "metallic" palladium particles. The initial increase in methane conversion is followed by a temporary minimum as oxygen introduction first leads to the formation of a chemisorbed oxygen layer on the palladium crystallites. This is detected by a rapid increase in Pd^{2+} fraction from a low level to approximately 25%, which corresponds well with the palladium dispersion (20%) for this catalyst. The results are in line with previous studies where a low catalytic activity for methane oxidation has been correlated to an oxygen saturated surface of the palladium particles [61,128–130]. The temporary minimum is most pronounced in the experiment with the lowest temperature and oxygen concentration (top left panel of Figure 5.2). In comparison to experiments performed at higher oxygen concentrations and temperatures, a significantly slower increase in Pd^{2+} fraction is here seen after the initial increase to 25%, barely reaching 40% at the end of the net-oxidizing period. At 360 °C and
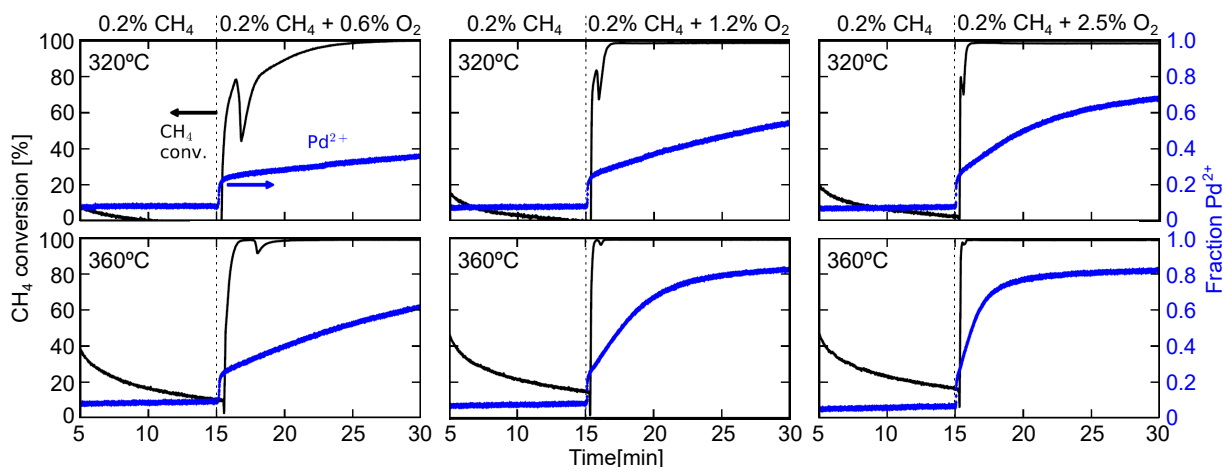
Figure 5.2: Methane conversion and fraction of oxidised Pd during oxygen step-response experiments over 5 wt.% Pd/Al_2O_3 by addition of 0.6 (left), 1.2 (middle), and 2.5% (right) O_2 to a feed of 0.2 vol.% CH_4 at 320 (top) and 360 °C (bottom).

2.5% oxygen present, the corresponding Pd^{2+} fraction is twice as high. This second oxidation regime corresponds to a deeper (bulk) oxidation of palladium crystallites. The temperature and oxygen concentrations trends are in accordance to previous findings [131, 132], and the large drop in methane conversion observed in the top left panel is due to the long time required to form an active bulk palladium oxide phase.

The effects of water vapor and temperature on the palladium oxidation state and catalytic activity were studied in **Paper V**. As displayed in the left panels of Figure 5.3, the methane TOF increases with increased temperature in dry conditions over a 2 wt.% Pd/Al_2O_3 catalyst with high dispersion (Pd/Al_2O_3-$D_{57\%}$). Independent of reaction temperature, an initial increase in Pd^{2+} fraction to about 50% is seen. Similar to the previous study on the 5 wt.% Pd/Al_2O_3 catalyst, this value corresponds well to the palladium dispersion. Again, higher temperature increases the rate of palladium bulk oxidation. However, after 15 and 45 min when oxygen is removed from the feed, both the TOF and Pd^{2+} fraction decrease rapidly. This is due to the inability of the catalytic system to regenerate oxygen vacancies in the PdO lattice, which leads to reduction to metallic palladium by methane. Over time, oxygen becomes a limiting reactant and the methane TOF decreases to low level. A zero level in Pd^{2+} fraction is however not reached, indicating that some palladium still interacts with oxygen atoms. One explanation to this could be the large number of palladium atoms in contact with the alumina through the large palladium-alumina interface for this highly dispersed sample.

In wet conditions a few differences are observed, see right panels of Figure 5.3.
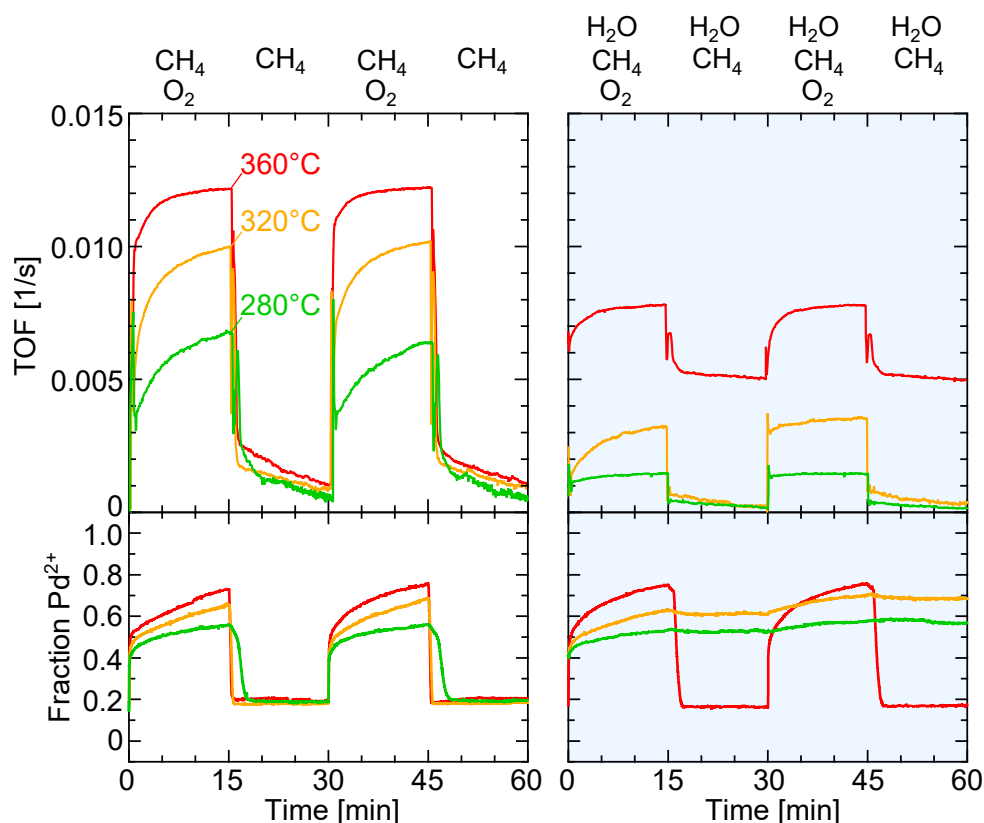
Figure 5.3: Oxidation of 0.1% CH_4 in the absence (left panels) and presence (right panels) of 1% H_2O over Pd/Al$_2$O$_3$-$D_{57\%}$ at 280 (green) 320 (orange) and 360 °C (red). 1.5% O_2 is turned on/off from the feed every 15th min.

The methane oxidation is generally inhibited by water and the TOF is lower in the presence of water vapor in all experimental conditions except during the oxygen-free steps (15-30 min and 45-60 min) at 360 °C. As discussed in section 3.2.1, a high concentration of carbon dioxide was detected in the outlet product stream in the absence of oxygen during a corresponding flow reactor test. At lower temperatures or in the absence of water, carbon monoxide was instead detected as the main product. This indicates a change in reaction mechanism from partial methane oxidation to methane steam reforming and subsequently the water-gas shift reaction is triggered by an elevated reaction temperature. The strong effect of reaction temperature in wet conditions is furthermore observed for the Pd^{2+} fraction in the absence of oxygen. At 280 and 320 °C, only a slight decrease in palladium oxidation state is seen in the beginning of a rich period. The Pd^{2+} fraction is then unaffected until the second oxygen step where the palladium particles are oxidised slightly more. The exception is again observed for the experiment performed at 360 °C, where a significant reduction as for dry conditions

50

occurs. Measurements with periodic oxygen and hydrogen exposure in wet conditions, included as supporting information in **Paper V**, confirm that the reduction of palladium oxide is dependent on temperature and water presence also when hydrogen is used as reductant. Although a 15 times higher concentration of hydrogen (1.5 %) was added to the feed compared to methane (0.1 %), a reaction temperature of 280 °C was not sufficient to reduce the palladium oxide particles in the presence of water. An explanation for this could be that a high coverage of surface-bound water or hydroxyl species on the catalyst prevent the reductant from dissociative adsorption by blocking specific sites where it otherwise preferentially dissociates and reacts with lattice oxygen.

5.3.2   Influence of catalyst formulation

The top panels in Figure 5.4 reveal that the methane TOF is higher for the two ZSM-5 supported catalysts compared to the ones with Al_2O_3 support. Further, the catalyst with lowest palladium dispersion (Pd/ZSM-5-$D_{5.2\%}$) and largest palladium particles shows the highest TOF in both the absence and presence of water. The same trend is observed when comparing the two Al_2O_3 supported catalysts, where the catalytic activity is higher for Pd/Al_2O_3-$D_{14\%}$ compared to Pd/Al_2O_3-$D_{57\%}$. As discussed for Pd/Al_2O_3-$D_{57\%}$, an inhibiting effect of 1% water vapor is also observed for the catalysts with different supports and larger palladium particle size during the oxygen lean periods. Similarly, methane steam reforming occurs at 360 °C for all catalysts during the rich periods.

The bottom left panel of Figure 5.4 shows variations in Pd^{2+} fraction with changes in the oxygen-to-methane ratio for the four catalysts in dry conditions. Similar to the previous results, a rapid increase in Pd^{2+} fraction followed by a gradual increase is observed when the reduced catalysts are exposed to oxygen. Depending on support material and palladium dispersion, the palladium particles are oxidized to different extent during the lean period. The highest Pd^{2+} fraction is reached for the two catalysts with the highest palladium dispersion. This indicates that the oxidation rate of palladium nanoparticles is related to the particle size and that smaller particles are bulk oxidized faster than larger ones. A similar Pd^{2+} fraction is furthermore obtained for the two catalysts with highest palladium dispersion, which is somewhat unexpected since an approximately three times smaller palladium particle size was measured for Pd/Al_2O_3-$D_{57\%}$. Also for the two catalysts with lowest palladium dispersion, a higher oxidation state is reached for the one with ZSM-5 support. This indicates that also the
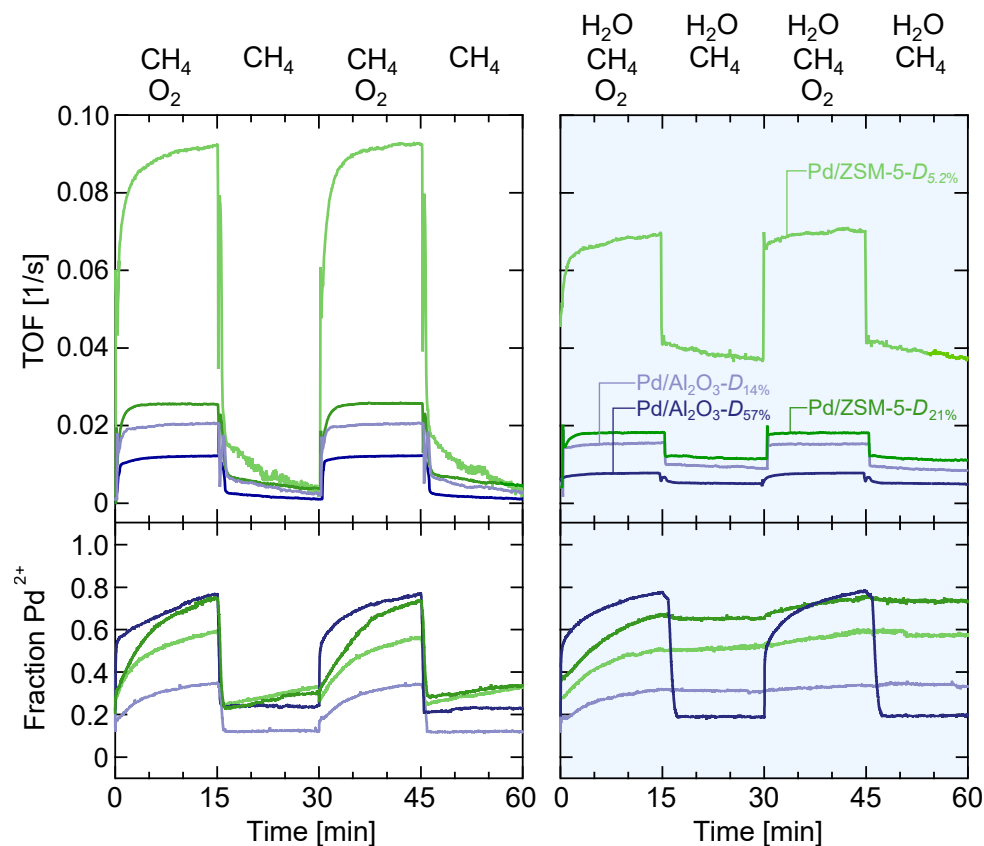
Figure 5.4: Oxidation of 0.1% CH_4 in the absence (left panels) and presence (right panels) of 1% H_2O over Pd/Al$_2$O$_3$-$D_{57\%}$ (dark blue), Pd/Al$_2$O$_3$-$D_{14\%}$ (light blue), Pd/ZSM-5-$D_{21\%}$ (dark green) and Pd/ZSM-5-$D_{5.2\%}$ (light green) at 360 °C. 1.5% O_2 is turned on/off from the feed every 15th min.

support material impacts the rate of palladium oxidation. A rapid decrease in palladium oxidation state is furthermore seen for all catalysts in the beginning of the methane rich periods. Approximately the same Pd^{2+} fraction is reached for all catalysts except for Pd/Al$_2$O$_3$-$D_{14\%}$ that appears to be slightly more reduced. For the ZSM-5 supported catalysts, a slow increase in Pd^{2+} fraction is in fact observed during the rich periods after the initial decrease. This behaviour has previously been observed in the presence of hydrocarbons, and explained by the formation of palladium carbide [133, 134]. The palladium carbide formation is however not observed during the rich periods in wet conditions, see bottom right panel of Figure 5.4. Like previously seen at lower temperatures for Pd/Al$_2$O$_3$-$D_{57\%}$, the presence of water in the feed hampers the reducing ability of methane for the three remaining catalysts. A reason why only Pd/Al$_2$O$_3$-$D_{57\%}$ is reduced at this temperature is likely related to the smaller palladium particle size and higher number of available surface sites for dissociative adsorption of methane for this catalyst.

CHAPTER 6

CATALYST DESIGN FOR IMPROVED WATER RESISTANCE

Based on the results from previous chapters, we have learned that both palladium particle size and choice of support material are important design parameters to consider when formulating methane oxidation catalysts with high resistance towards water inhibition. Figure 6.1, shows a long-term methane oxidation experiment performed in wet conditions over four different catalysts to emphasise the importance of these design parameters. The two catalysts prepared to have as high palladium dispersion as possible on Al_2O_3 and ZSM-5 (SAR 2000), i.e. Pd/Al_2O_3-$D_{57\%}$ and Pd/ZSM-5-$D_{21\%}$, perform equally well in dry conditions (0-30 min) where all methane is converted. A lower catalytic activity, reaching approximately 87% and 68% is observed for Pd/ZSM-5-$D_{5.2\%}$ and Pd/Al_2O_3-$D_{14\%}$, respectively, i.e. the two catalysts with lowest palladium dispersion. After 30 min, 10 vol.% water vapor is added to the reaction feed. A rapid drop in methane conversion is then observed for all examined catalysts. The largest drops are observed for the catalysts with alumina support. For the Al_2O_3 supported catalysts, the initial decrease is followed by a continuous decrease in methane conversion to a low level of 9 and 0% for Pd/Al_2O_3-$D_{57\%}$ and Pd/Al_2O_3-$D_{14\%}$ respectively. A significantly higher resistance towards water inhibition is seen for the ZSM-5 supported catalysts. The long-term decrease in methane conversion is not as pronounced, and the conversion remains on a relatively high level of 50% for Pd/ZSM-5-$D_{21\%}$ and 30% for Pd/ZSM-5-$D_{5.2\%}$ after 24 h exposure. Finally, when the water vapor is turned off, a regained catalytic activity to initial levels is seen for the ZSM-5 supported catalysts while left on a lower level for the two catalysts with alumina support.
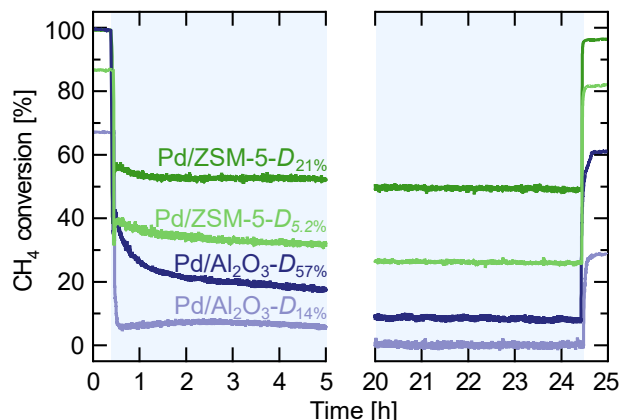
Figure 6.1: Methane conversion over Pd/Al$_2$O$_3$-$D_{57\%}$ (dark blue), Pd/Al$_2$O$_3$-$D_{14\%}$ (light blue), Pd/ZSM-5-$D_{21\%}$ (dark green) and Pd/ZSM-5-$D_{5.2\%}$ (light green) at 400 °C in 2% O$_2$ + 0.1% CH$_4$ (0-0.5 h), 2% O$_2$ + 0.1% CH$_4$ + 10% H$_2$O (0.5-24.5 h) and 2% O$_2$ + 0.1% CH$_4$ (24.5-25 h).

The long-term experiment in wet conditions stress the importance of a suitable support material. As seen for the alumina supported catalysts that traditionally are used for methane oxidation in vehicle applications, an accumulation of surface hydroxyl species over time leads to a low catalytic activity. The Pd/Al$_2$O$_3$-$D_{14\%}$ sample here represents a catalyst that has been operating in an abatement system for several years. For such catalyst, the initially small palladium particles have sintered to larger ones, and its performance in realistic conditions is far from adequate. Non-satisfactory performance is also revealed for the Al$_2$O$_3$ supported catalyst with the highest palladium dispersion. Pd/Al$_2$O$_3$-$D_{57\%}$ represents a fresh catalyst where the palladium particle size is on the lower side of the nanometre scale. The poor performance for this catalyst in the presence of water is in line with results from the catalytic methane oxidation chapter where increased activation energies and turnover frequencies were disclosed over too small palladium particles on alumina. For the ZSM-5 supported catalysts, a higher methane conversion is seen for the one with highest palladium dispersion. To make any further recommendations regarding an optimal palladium particle size for methane oxidation in wet conditions over this type of formulation, a more thorough investigation is required. Model catalysts with ZSM-5 support for such study may resemble the Al$_2$O$_3$ supported ones in **Paper I** prepared with different palladium loadings and calcination temperatures.

CHAPTER 7

CONCLUDING REMARKS

The main focus of this thesis has been to investigate the inhibiting effect of water vapor on the total oxidation of methane over supported palladium-based catalysts. Various types of model catalysts have been prepared using different Pd loadings, calcination conditions and support materials. The samples were thoroughly characterised with different techniques and tested for their ability to oxidise methane in the absence and presence of water vapor. Transient *operando* spectroscopy measurements were in addition performed to monitor changes in the coverage of surface-bound species and Pd oxidation state, and enable correlations to catalytic activity.

Methane oxidation kinetics

The kinetics for catalytic methane oxidation over Pd/γ-Al_2O_3 samples with similar Pd surface area but different Pd dispersion was thoroughly studied from the conversion profiles of methane in dry and wet conditions. The results showed an increased apparent activation energy with increasing palladium particle size in dry conditions, whereas the energy barrier decreased in wet conditions. We suggest that PdO sites at the rim of the palladium oxide particles in contact with the alumina support play an important role for the activation process. This was especially observed in dry conditions where the TOF was high and the apparent activation was low for catalysts with a high fraction of Pd-Al_2O_3 rim sites. It was however shown that these rim sites were considerably less tolerant to water, likely caused by a high coverage of hydroxyl species which prevents them to participate in the reaction. A lower apparent activation energy was instead,

in the presence of water, observed for catalysts with larger Pd particles and a higher fraction of sites located solely on the PdO particles. Hence, we suggest that the targeted palladium particle size for methane oxidation catalysts with increased water resistance, should not be smaller than approximately 2 nm.

Surface-bound hydroxyls

The evolution of IR-bands associated with linear and bridge-bonded types of hydroxyls on alumina were observed when Pd/Al$_2$O$_3$ catalysts were exposed to various mixtures of oxygen, methane, and water. The hydroxyl build-up during methane oxidation in wet conditions can be divided into two regimes, starting with a rapidly increased coverage that settles after a few minutes. A slow continuous accumulation is then observed over time. It was also shown that methane oxidation in itself provided an additional formation route of surface hydroxyls than the ones evolved by water dissociation. These hydroxyls are expected to be located close the PdO particles, such as the PdO-Al$_2$O$_3$ rim. No surface-bound hydroxyls were however detected on PdO during methane oxidation in neither the absence nor presence of water, although the catalytic activity was clearly lower in wet conditions. This does not necessarily confirm a non-existent or an utterly low hydroxyl coverage since the lack of absorption bands also could be due to a low surface area and/or poor reflectivity of the PdO powder sample. Moreover, for bare γ-Al$_2$O$_3$ and the Pd/γ-Al$_2$O$_3$ catalyst calcined at 900 °C, two additional hydroxyl bands, not observed for catalysts calcined at lower temperatures, appeared upon water exposure. These bands were assigned to suppressed vibrations of linearly bonded hydroxyls as adjacent species started to interact with each other when the coverage increased. Since this was not observed for catalysts with high palladium dispersion, it seems like palladium that preferentially occupies corresponding Lewis acid sites on the alumina surface decreases due to sintering at high temperature treatment.

Palladium oxidation state

With the understanding of methane oxidation in oxygen excess obtained from activity tests and infrared spectroscopy measurements, *operando* XAS experiments instead revealed how changes in reaction temperature, oxygen concentration, and presence of water vapor affect the oxidation state of supported palladium particles. Generally, a rapidly increased methane conversion and palladium oxidation state was observed

when oxygen was added to a dry feed of methane. This was associated to a high catalytic activity over metallic palladium particles. For Pd/γ-Al$_2$O$_3$, a temporary minimum in catalytic activity was then observed as oxygen was chemisorbed on metallic palladium. This step was followed by a regenerated catalytic activity as the palladium particle was bulk oxidised. The duration of the minimum was related to the oxidation rate of palladium, which in turn increased with increased reaction temperature and oxygen concentration. When oxygen is switched off from the dry feed, a rapid decrease in catalytic activity and palladium oxidation state is observed independently off reaction temperature. In the presence of water vapor however, the decrease in oxidation state is more or less unaffected when oxygen is turned off at temperatures lower than 360 °C. One explanation to this result could be that hydroxyls adsorbed on the palladium oxide impede methane dissociation and subsequent surface reaction with lattice oxygen, which impairs the reduction ability.

Support effects

A promoted catalytic activity in terms of increased apparent methane TOF was observed over alumina supported palladium oxide particles compared to bare PdO powder. An even higher methane TOF was furthermore observed in all *operando* XAS experiments for catalysts with ZSM-5 (SAR-2000) support. Pd/ZSM-5 catalysts are hence very promising for future applications in emission control. The long term experiments performed in realistic conditions strengthen the idea of a more durable Pd/ZSM-5 catalyst formulation for methane oxidation compared to Pd/γ-Al$_2$O$_3$ that traditionally is used.

Acknowledgements

I would also like to thank:

My main supervisor Per-Anders Carlsson and co-supervisor Magnus Skoglundh for your great support over the years. It has been a very instructive and satisfying period of my life, and I really appreciate that you always have been there to help when needed.

Agnes Raj, David Thompsett and Gudmund Smedler for constructive meetings, creative ideas and showing genuine interest in my latest research results.

Hanna Härelind, Anders Palmqvist, Carina Jogevik, Frida Andersson, Lotta Pettersson and Ann Jakobsson for administrative help and all fun and well-organized events.

Lasse, Lennart and Ulf for all your help in the reactor lab and the joyful spirit you bring.

Andreas Schaefer, Anne Wendel and Mats Hulander for creating a nice and safe working environment, and that you always are there to help us out when problems arise.

All the colleagues (past and present) at TYK and KCK for the pleasant working environment and the fun we have both at and outside Chalmers.

My wonderful and supportive girlfriend Josefin for brighten up my life.

Last but not the least, my mom and my dad for always being there for me.

BIBLIOGRAPHY

[1] C. Le Quéré, R. Andrew, P. Friedlingstein, S. Sitch, J. Pongratz, A. Manning, and D. Zhu, *Earth System Science Data*, 2018, **10**, 405–448.

[2] T. Lenton, J. Rockström, O. Gaffney, S. Rahmstorf, K. Richardson, W. Steffen, and H. J. Shellnhuber, *Nature*, 2019, **575**, 592–595.

[3] *World Energy Outlook*, International Energy Agency, 2019.

[4] M. Imran, T. Yasmin, and A. Shakoor, *Renewable and Sustainable Energy Reviews*, 2015, **51**, 785–797.

[5] P. Bielaczyc, A. Szczotka, and J. Woodburn, *IOP Conference Series: Materials Science and Engineering*, 2016, **148**(1).

[6] M. E. Stettler, W. J. Midgley, J. J. Swanson, D. Cebon, and A. M. Boies, *Environmental Science and Technology*, 2016, **50**(4), 2018–2026.

[7] T. Korakianitis, A. M. Namasivayam, and R. J. Crookes, *Progress in Energy and Combustion Science*, 2011, **37**(1), 89–112.

[8] A. Petersson and A. Wellinger, *IEA Bioenergy*, 2009, **Task 37**, 1–20.

[9] J. L. Osorio-Tejada, E. Llera-Sastresa, and S. Scarpellini, *Renewable and Sustainable Energy Reviews*, 2017, **71**, 785–795.

[10] A. Sanches-Pereira and M. F. Gómez, *Journal of Cleaner Production*, 2015, **96**, 452–466.

[11] R. Chandra, V. K. Vijay, P. M. Subbarao, and T. K. Khura, *Applied Energy*, 2011, **88**(11), 3969–3977.

[12] IEA, *CO2 Emissions from Fuel Combustion 2017*, OECD Publishing Paris, 2017.

[13] O. Edenhofer, R. Pichs-Madruga, Y. Sokona, E. Farahani, S. Kadner, K. Sey-both, A. Adler, I. Baum, S. Brunner, P. Eickemeier, B. Kriemann, J. Savolainen, S. Schlömer, C. von Stechow, T. Zwickel, and J. Minx Climate Change 2014: Mitigation of Climate Change Technical report, Cambridge University Press, 2014.

[14] W. Martin and M. Ray, *The ICCT Briefing Paper*, 2016, **1**, 1–17.

[15] D. H. Everett, *Pure and Applied Chemistry*, 1972, **31**(4), 577–638.

[16] A. R. Matthias Beller and R. A. van Santen, *Catalysis: From Principles to Applications*, Wiley-VCH, 2012.

[17] R. Schlögl, *Angewandte Chemie - International Edition*, 2015, **54**(11), 3465–3520.

[18] M. Van Den Bossche and H. Grönbeck, *Journal of the American Chemical Society*, 2015, **137**(37), 12035–12044.

[19] R. Burch, F. Urbano, and P. Loader, *Applied Catalysis A: General*, 1995, **123**(1), 173–184.

[20] A. Trinchero, A. Hellman, and H. Grönbeck, *Surface Science*, 2013, **616**, 206–213.

[21] A. J. Medford, A. Vojvodic, J. S. Hummelshøj, J. Voss, F. Abild-Pedersen, F. Studt, T. Bligaard, A. Nilsson, and J. K. Nørskov, *Journal of Catalysis*, 2015, **328**, 36–42.

[22] R. Burch, D. J. Crittle, and M. J. Hayes, *Catalysis Today*, 1999, **47**, 229–234.

[23] A. A. Latimer, A. R. Kulkarni, H. Aljama, J. H. Montoya, J. S. Yoo, C. Tsai, F. Abild-Pedersen, F. Studt, and J. K. Nørskov, *Nature Materials*, 2016, **1**, 1–6.

[24] M. Trueba and S. P. Trasatti, *European Journal of Inorganic Chemistry*, 2005, **2005**, 3393–3403.

[25] R. Gholami, M. Alyani, and K. Smith, *Catalysts*, 2015, **5**(2), 561–594.

[26] J. Lampert, M. Kazi, and R. Farrauto, *Applied Catalysis B: Environmental*, 1997, **14**, 211–223.

[27] J. C. van Giezen, F. R. van den Berg, J. L. Kleinen, A. J. van Dillen, and J. W. Geus, *Catalysis Today*, 1999, **47**, 287–293.

[28] P. Gélin, L. Urfels, M. Primet, and E. Tena, *Catalysis Today*, 2003, **83**(1-4), 45–57.

[29] K. Persson, L. D. Pfefferle, W. Schwartz, A. Ersson, and S. G. Järås, *Applied Catalysis B: Environmental*, 2007, **74**, 242–250.

[30] M. Monai, T. Montini, C. Chen, E. Fonda, R. J. Gorte, and P. Fornasiero, *ChemCatChem*, 2015, **7**(14), 2038–2046.

[31] C. H. Bartholomew, *Applied Catalysis A: General*, 2001, **212**(1-2), 17–60.

[32] A. Morlang, U. Neuhausen, K. V. Klementiev, F. W. Schütze, G. Miehe, H. Fuess, and E. S. Lox, *Applied Catalysis B: Environmental*, 2005, **60**(3-4), 191–199.

[33] G. Lapisardi, L. Urfels, P. Gélin, M. Primet, A. Kaddouri, E. Garbowski, S. Toppi, and E. Tena, *Catalysis Today*, 2006, **117**(4), 564–568.

[34] J. Englund, K. Xie, S. Dahlin, A. Schaefer, D. Jing, S. Shwan, L. Andersson, P.-A. Carlsson, L. J. Pettersson, and M. Skoglundh, *Catalysts*, 2019, **9**(12), 1014.

[35] A. Chakrabarti, M. E. Ford, D. Gregory, R. Hu, C. J. Keturakis, S. Lwin, Y. Tang, Z. Yang, M. Zhu, M. A. Bañares, and I. E. Wachs, *Catalysis Today*, 2017, **283**, 27–53.

[36] A. Urakawa, *Current Opinion in Chemical Engineering*, 2016, **12**, 31–36.

[37] M. Boudart, *Topics in Catalysis*, 2000, **13**(1-2), 147–149.

[38] K. P. de Jong, *Synthesis of Solid Catalysts*, Wiley-VCH, 2009.

[39] P. Munnik, P. E. De Jongh, and K. P. De Jong, *Chemical Reviews*, 2015, **115**(14), 6687–6718.

[40] J. P. Brunelle, *Pure and Applied Chemistry*, 1978, **50**(9-10), 1211–1229.

[41] R. J. HUNTER, *Zeta Potential in Colloid Science: Principles and Applications*, Elsevier Ltd., 1981.

[42] D. C. Harris, *Quantitative Chemical Analysis*, W. H. Freeman and Company, 2010.

[43] C. Streli, P. Wobrauschek, and P. Kregsamer in *Encyclopedia of Spectroscopy and Spectrometry (Third Edition)*, ed. J. C. Lindon, G. E. Tranter, and D. W. Koppenaal; Academic Press, Oxford, third edition ed., 2017; pp. 707 – 715.

[44] P. H. Emmett, *Journal of the American Chemical Society*, 1936, **60**(2), 309–319.

[45] I. Langmuir, *Journal of the American Chemical Society*, 1918, **40**(9), 1361–1403.

[46] K. S. Sing, *Advances in Colloid and Interface Science*, 1998, **76-77**, 3 – 11.

[47] P. A. Webb and C. Orr, *Analytical Methods in Fine Particle Technology*, Micromeritics Instrument Corporation, 1997.

[48] P. Canton, G. Fagherazzi, M. Battagliarin, F. Menegazzo, F. Pinna, and N. Pernicone, *Langmuir*, 2002, **18**, 6530–6535.

[49] D. Tessier, A. Rakai, and F. Bozon-Verduraz, *Journal of the Chemical Society, Faraday Transactions*, 1992, **88**(5), 741–749.

[50] T. Lear, R. Marshall, J. A. Lopez-Sanchez, S. D. Jackson, T. M. Klapötke, M. Bäumer, G. Rupprechter, H. J. Freund, and D. Lennon, *Journal of Chemical Physics*, 2005, **123**(17), 174706.

[51] S. D. Ebbesen, B. L. Mojet, and L. Lefferts, *Physical Chemistry Chemical Physics*, 2009, **11**(4), 641–649.

[52] S. J. Pennycook and P. D. Nellist, *Scanning Transmission Electron Microscopy*, Springer-Verlag New York, 2011.

[53] X. Zhang, J. Meng, B. Zhu, J. Yu, S. Zou, Z. Zhang, Y. Gao, and Y. Wang, *Chemical Communications*, 2017, **53**(99), 13213–13216.

[54] W. P. Yant and C. O. Hawk, *Journal of the American Chemical Society*, 1927, **49**(6), 1454–1460.

[55] R. B. Anderson, K. C. Stein, J. J. Feenan, and L. J. E. Hofer, *Industrial & Engineering Chemistry*, 1961, **53**(10), 809–812.

[56] R. F. Hicks, H. Qi, M. L. Young, and R. G. Lee, *Journal of Catalysis*, 1990, **122**(2), 295–306.

[57] S. T. Kolaczkowski, W. J. Thomas, J. Titiloye, and D. J. Worth, *Combustion Science and Technology*, 1996, **118**(1-3), 79–100.

[58] G. Zhu, J. Han, D. Y. Zemlyanov, and F. H. Ribeiro, *Journal of Physical Chemistry B*, 2005, **109**(6), 2331–2337.

[59] A. Hellman, A. Resta, N. M. Martin, J. Gustafson, A. Trinchero, P. A. Carlsson, O. Balmes, R. Felici, R. Van Rijn, J. W. Frenken, J. N. Andersen, E. Lundgren, and H. Grönbeck, *Journal of Physical Chemistry Letters*, 2012, **3**(6), 678–682.

[60] S. K. Matam, M. H. Aguirre, A. Weidenkaff, and D. Ferri, *Journal of Physical Chemistry C*, 2010, **114**(20), 9439–9443.

[61] N. M. Martin, M. Van Den Bossche, A. Hellman, H. Grönbeck, C. Hakanoglu, J. Gustafson, S. Blomberg, N. Johansson, Z. Liu, S. Axnanda, J. F. Weaver, and E. Lundgren, *ACS Catalysis*, 2014, **4**(10), 3330–3334.

[62] J. R. McBride, K. C. Hass, and W. H. Weber, *Physical Review B*, 1991, **44**, 5016–5028.

[63] E. Lundgren, J. Gustafson, A. Mikkelsen, J. N. Andersen, A. Stierle, H. Dosch, M. Todorova, J. Rogal, K. Reuter, and M. Scheffler, *Physical Review Letters*, 2004, **92**, 046101.

[64] A. Stierle, N. Kasper, H. Dosch, E. Lundgren, J. Gustafson, A. Mikkelsen, and J. N. Andersen, *Journal of Chemical Physics*, 2005, **122**(4), 1–6.

[65] M. Blanco-Rey and S. J. Jenkins, *Journal of Chemical Physics*, 2009, **130**(1).

[66] N. Seriani, J. Harl, F. Mittendorfer, and G. Kresse, *Journal of Chemical Physics*, 2009, **131**(5).

[67] J. F. Weaver, C. Hakanoglu, J. M. Hawkins, and A. Asthagiri, *Journal of Chemical Physics*, 2010, **132**(2).

[68] A. Antony, A. Asthagiri, and J. F. Weaver, *Journal of Chemical Physics*, 2013, **139**(10).

[69] M. McEntee, W. Tang, M. Neurock, and J. T. Yates, *ACS Catalysis*, 2015, **5**(2), 744–753.

[70] T. P. Senftle, A. C. Van Duin, and M. J. Janik, *ACS Catalysis*, 2017, **7**(1), 327–332.

[71] T. K. Slot, D. Eisenberg, and G. Rothenberg, *ChemCatChem*, 2018, **10**(10), 2119–2124.

[72] F. Dhainaut and P. Granger, *Topics in Catalysis*, 2019, **62**(1-4), 331–335.

[73] G. Jacobs, P. M. Patterson, Y. Zhang, T. Das, J. Li, and B. H. Davis, *Applied Catalysis A: General*, 2002, **233**(1-2), 215–226.

[74] S. Storsæter, B. Tøtdal, J. C. Walmsley, B. S. Tanem, and A. Holmen, *Journal of Catalysis*, 2005, **236**(1), 139–152.

[75] S. Mosallanejad, B. Z. Dlugogorski, E. M. Kennedy, and M. Stockenhuber, *ACS Omega*, 2018, **3**(5), 5362–5374.

[76] M. Jørgensen and H. Grönbeck, *ACS Catalysis*, 2017, **7**(8), 5054–5061.

[77] M. Boudart, *Chemical Reviews*, 1995, **95**(3), 661–666.

[78] C. Muller, M. Maciejewski, R. A. Koeppel, A. Baiker, C. A. Müller, M. Maciejewski, R. A. Koeppel, and A. Baiker, *Catalysis Today*, 1999, **47**(1-4), 245–252.

[79] A. E. Yarulin, R. M. Crespo-Quesada, E. V. Egorova, and L. L. Kiwi-Minsker, *Kinetics and Catalysis*, 2012, **53**(2), 253–261.

[80] A. M. Batkin, N. S. Teleguina, G. O. Bragina, V. I. Zaikovsky, I. P. Prosvirin, A. K. Khudorozhkov, and V. I. Bukhtiyarov, *Topics in Catalysis*, 2013, **56**, 306–310.

[81] L. Li, F. Abild-Pedersen, J. Greeley, and J. K. Nørskov, *Journal of Physical Chemistry Letters*, 2015, **6**(19), 3797–3801.

[82] K. Murata, Y. Mahara, J. Ohyama, Y. Yamamoto, S. Arai, and A. Satsuma, *Angewandte Chemie International Edition*, 2017, **8520**, 15993–15997.

[83] P. Velin, M. Ek, M. Skoglundh, A. Schaefer, A. Raj, D. Thompsett, G. Smedler, and P.-A. Carlsson, *The Journal of Physical Chemistry C*, 2019, **123**(42), 25724–25737.

[84] Y.-F. Y. Yao, *Industrial and Engineering Chemistry Product Research and Development*, 1980, **19**(3), 293–298.

[85] M. R. Lyubovsky and L. D. Pfefferle, *Catalysis Today*, 1999, **47**(1-4), 29–44.

[86] R. E. Hayes, S. T. Kolaczkowski, P. K. C. Li, and S. Awdry, *Chemical Engineering Science*, 2001, **56**, 4815–4835.

[87] R. Kikuchi, S. Maeda, K. Sasaki, S. Wennerström, and K. Eguchi, *Applied Catalysis A: General*, 2002, **232**(1-2), 23–28.

[88] C. F. Cullis and B. M. Willatt, *Journal of Catalysis*, 1983, **83**(2), 267–285.

[89] M. Zheng and E. Mirosh, *Chemical Engineering Science*, 2001, **56**(8), 2641–2658.

[90] M. Haruta and M. Daté, *Applied Catalysis A: General*, 2001, **222**(1-2), 427–437.

[91] D. Bounechada, S. Fouladvand, L. Kylhammar, T. Pingel, E. Olsson, M. Skoglundh, J. Gustafson, M. Di Michiel, M. A. Newton, and P.-A. Carlsson, *Physical Chemistry Chemical Physics*, 2013, **15**(22), 8648–8661.

[92] I. Czekaj, K. A. Kacprzak, and J. Mantzaras, *Physical Chemistry Chemical Physics*, 2013, **15**(27), 11368.

[93] S. Fouladvand, M. Skoglundh, and P.-A. Carlsson, *Catalysis Science & Technology*, 2014, **4**(10), 3463–3473.

[94] Y. Suchorski, S. M. Kozlov, I. Bespalov, M. Datler, D. Vogel, Z. Budinska, K. M. Neyman, and G. Rupprechter, *Nature Materials*, 2018, **17**(6), 519–522.

[95] H. Günzler and H.-U. Gremlich, *IR Spectroscopy - An Introduction*, WILEY-VCH, 2002.

[96] Z. M. Khoshhesab, *Reflectance IR Spectroscopy*, InTech, 2012.

[97] J. W. Niemantverdriet, *Spectroscopy in Catalysis: An Introduction*, Wiley-VCH Verlag GmbH & Co. KGaA, 2007.

[98] F. C. Meunier, *Reaction Chemistry & Engineering*, 2016, **1**(2), 134–141.

[99] H. Li, M. Rivallan, F. Thibault-Starzyk, A. Travert, and F. C. Meunier, *Physical Chemistry Chemical Physics*, 2013, **15**(19), 7321.

[100] P. Gelin, A. R. Siedle, and J. T. Yates, *The Journal of Physical Chemistry*, 2005, **88**(14), 2978–2985.

[101] S. Zou, R. Gómez, and M. J. Weaver, *Journal of Electroanalytical Chemistry*, 1999, **474**(2), 155–166.

[102] G. Rupprechter, T. Dellwig, H. Unterhalt, and H.-J. Freund, *The Journal of Physical Chemistry B*, 2002, **105**(18), 3797–3802.

[103] Y. G. Yan, Q. X. Li, S. J. Huo, M. Ma, W. B. Cai, and M. Osawa, *Journal of Physical Chemistry B*, 2005, **109**(16), 7900–7906.

[104] D. Ciuparu and L. Pfefferle, *Applied Catalysis A: General*, 2001, **209**(1-2), 415–428.

[105] D. Ciuparu and L. Pfefferle, *Catalysis Today*, 2002, **77**(3), 167–179.

[106] D. Ciuparu, E. Perkins, and L. Pfefferle, *Applied Catalysis A: General*, 2004, **263**(2), 145–153.

[107] W. R. Schwartz and L. D. Pfefferle, *Journal of Physical Chemistry C*, 2012, **116**(15), 8571–8578.

[108] A. A. Tsyganenko and V. N. Filimonov, *Spectroscopy Letters*, 1972, **5**(12), 477–487.

[109] H. Knözinger and P. Ratnasamy, *Catalysis Reviews*, 1978, **17**(1), 31–70.

[110] G. Busca, V. Lorenzelli, G. Ramis, and R. J. Willey, *Langmuir*, 1993, **9**(6), 1492–1499.

[111] M. Digne, P. Sautet, P. Raybaud, P. Euzen, and H. Toulhoat, *Journal of Catalysis*, 2002, **211**(1), 1–5.

[112] M. Digne, P. Sautet, P. Raybaud, P. Euzen, and H. Toulhoat, *Journal of Catalysis*, 2004, **226**(1), 54–68.

[113] G. Busca, *Catalysis Today*, 2014, **226**, 2–13.

[114] A. B. M. Saad, V. A. Ivanov, J. C. Lavalley, P. Nortier, and F. Luck, *Applied Catalysis A, General*, 1993, **94**(1), 71–83.

[115] N. Sadokhina, F. Ghasempour, X. Auvray, G. Smedler, U. Nylén, M. Olofsson, and L. Olsson, *Catalysis Letters*, 2017, **147**(0), 2360–2371.

[116] A. Gremminger, P. Lott, M. Merts, M. Casapu, J. D. Grunwaldt, and O. Deutschmann, *Applied Catalysis B: Environmental*, 2017, **218**, 833–843.

[117] Y. Li and J. N. Armor, *Applied Catalysis B, Environmental*, 1994, **3**(4), 275–282.

[118] H. Maeda, Y. Kinoshita, K. Reddy, K. Muto, S. Komai, N. Katada, and M. Niwa, *Applied Catalysis A: General*, 1997, **163**, 59–69.

[119] C.-K. Shi, L.-F. Yang, Z.-C. Wang, X. He, J.-X. Cai, G. Li, and X.-S. Wang, *Science*, 2003, **243**, 379–388.

[120] C. Shi, L. Yang, and J. Cai, *Fuel*, 2007, **86**(1-2), 106–112.

[121] Stefan Hüfner, *Photoelectron Spectroscopy Principles and Applications*, Springer-Verlag Berlin Heidelberg GmbH, 3rd ed., 2003.

[122] K. Mudiyanselage and D. J. Stacchiola, in *In-situ Characterization of Heterogeneous Catalysts*, John Wiley & Sons Ltd, 2013; chapter 8, pp. 209–239.

[123] S. Calvin, *XAFS for Everyone*, Boca Raton: CRC Press, 2013.

[124] S. Pascarelli, G. Aquilanti, L. Dubrovinsky, G. Guilera, O. Mathon, M. Munoz, M. A. Newton, M. Pasquale, A. Trapananti, E. Synchrotron, R. Facility, and J. Horowitz In *AIP Conference Proceedings*, Vol. 882, pp. 608–612, 2007.

[125] S. Pascarelli, O. Mathon, T. Mairs, I. Kantor, G. Agostini, and C. Strohm, *Journal of Synchrotron Radiation*, 2016, **23**, 353–368.

[126] G. Agostini, D. Meira, M. Monte, H. Vitoux, A. Iglesias-Juez, M. Fernandez-Garcia, O. Mathon, F. Meunier, G. Berruyer, F. Perrin, S. Pasternak, T. Mairs, S. Pascarelli, and B. Gorges, *Journal of Synchrotron Radiation*, 2018, **25**(6), 1745–1752.

[127] J. Keating, G. Sankar, T. Hyde, S. Koharac, and K. Ohara, *Physical Chemistry Chemical Physics*, 2013, **15**, 8555–8565.

[128] Y. H. Chin, C. Buda, M. Neurock, and E. Iglesia, *Journal of the American Chemical Society*, 2013, **135**(41), 15425–15442.

[129] X. Weng, H. Ren, M. Chen, and H. Wan, *ACS Catalysis*, 2014, **4**(8), 2598–2604.

[130] P. A. Carlsson, E. Fridell, and M. Skoglundh, *Catalysis Letters*, 2007, **115**(1-2), 1–7.

[131] J. Nilsson, P.-A. Carlsson, S. Fouladvand, N. M. Martin, J. Gustafson, M. A. Newton, E. Lundgren, H. Grönbeck, and M. Skoglundh, *ACS Catalysis*, 2015, **5**(4), 2481–2489.

[132] J. Nilsson, P. A. Carlsson, N. M. Martin, E. C. Adams, G. Agostini, H. Grönbeck, and M. Skoglundh, *Journal of Catalysis*, 2017, **356**, 237–245.

[133] J. A. Mccaulley, *Physical Review B*, 1993, **47**(9), 4873–4879.

[134] J. Nilsson, P. A. Carlsson, N. M. Martin, P. Velin, D. M. Meira, H. Grönbeck, and M. Skoglundh, *Catalysis Communications*, 2018, **109**(December 2017), 24–27.